LIBRARY
NAVAL POSTGRADUATE SCHOOL
MONTEREY, CALIF. 93940

MEASUREMENT OF AXIAL VELOCITY PROFILES

AND RESULTING ACOUSTICAL FIELDS

OF A ROD

APPROVED BY SUPERVISORY COMMITTEE:

TO

MY FAMILY

MEASUREMENT OF AXIAL VELOCITY PROFILES AND RESULTING ACOUSTICAL FIELDS OF A ROD

by

LIONEL JEROME NOWOTNY, B.S.

DISSERTATION

Presented to the Faculty of the Graduate School of

The University of Texas at Austin

in Partial Fulfillment

of the Requirements

for the Degree of

DOCTOR OF PHILOSOPHY

THE UNIVERSITY OF TEXAS AT AUSTIN

December, 1971

Thesis
.N946

ACKNOWLEDGEMENTS

The author wishes to express his deep appreciation to Dr. Elmer L. Hixson for serving as his supervising professor. His many suggestions and encouragements greatly contributed to the completion of this work. Thanks also go to Dr. C. W. Horton, Sr., Dr. F. X. Bostick, and Dr. O. M. Friedrich, Jr. for serving on the dissertation committee.

Appreciation is expressed to the Naval Underwater Research and Development Center, San Diego, California, and to the Applied Research Laboratories at Austin, Texas for generous assistance in providing equipment, funds and advice necessary to complete this project. The author also is indebted to the Naval Training Device Center at Orlando, Florida for their contribution of time, talent and equipment. Sincere thanks also go to Dr. G. W. Maxwell for supplying digital programs and advice pertinent to this endeavor.

The writer also wishes to express his gratitude to The University of Texas at Austin, Department of Electrical Engineering, The Office of Naval Research, The Armed Forces Joint Services Electronics Project and especially the U. S. Naval Ship Systems Command for their support of this work.

December, 1971 LJN

MEASUREMENT OF AXIAL VELOCITY PROFILES

AND RESULTING ACOUSTICAL FIELDS

OF A ROD

Publication No.___

Lionel Jerome Nowotny, Ph.D.
The University of Texas at Austin, 1971

Supervising Professor: Elmer L. Hixson

Sinusoidal stress waves over the frequency range 10-100 KHz were transmitted down a cylindrical aluminum rod twelve feet long and one and one-half inches in diameter. Using a modified Twyman-Green interferometer and a high sensitivity, fast rise time photo-diode radial distributions of axial displacement were measured at the radiating face of the rod while it was under continuous-wave excitation. Measurements verified the almost piston-like displacement profiles for low frequencies and indicated increased distortion of the face with increasing frequency. Nodal cylinders of axial displacement in the rod were found to occur beginning at about 30 KHz with only the lowest symmetric mode propagating in the rod.

The directivity pattern of the radiating rod was measured over the specified frequency range in the 28' x 18' x 15' deep pool of the Underwater Acoustics Laboratory Facility of The University of Texas. Only the radiating rod face was exposed to water at the plane surface of a 5' x 5' aluminum

baffle. Measurements taken, with pulsed sinusoidal excitation applied, indicated a considerable difference between radiation patterns of the rod and radiation patterns calculated for an ideal piston in an infinite baffle beginning at approximately 30 KHz.

TABLE OF CONTENTS

		Page
ABSTRACT		v
TABLE OF CONTENTS		vii
LIST OF FIGURES		ix
LIST OF PLATES		xi
LIST OF TABLES		xii
CHAPTER		
I	INTRODUCTION	
	A. Statement of the Problem	1
	B. Historical Background	2
	C. Format of the Paper	4
II	EVOLUTION OF THE EXPERIMENTAL METHOD	
	A. The Optimum Experiment	5
	1.) Description of the system	
	2.) Acoustic signal generation	
	3.) Timing of the acoustic signal	
	4.) The hydrophone and its circuitry	
	5.) The holographic system	
	B. Modifications of the Experiment Dictated by Physics and Facilities	19
	C. Final Test Method Used	26
III	THE EXPERIMENT	
	A. Measurement of Displacement Profiles	27

B. Measurement of Directivity Pattern 38

1.) The signal generation circuit

2.) The cylindrical rod assembly

3.) The pressure sensing system

IV THE EXPERIMENTAL RESULTS

A. Displacement Profiles and Discussion 47

B. Pressure Distributions and Discussion 65

V CONCLUSIONS AND RECOMMENDATIONS

A. Summary of Experimental Results 77

B. Areas for Fruitful Further Research 78

APPENDIX I DIGITAL PROGRAM "FIELDS" 79

BIBLIOGRAPHY 91

VITA

LIST OF FIGURES

Figure	Title	Page
1.	Vibrating Rod and Housing Assembly	6
2.	Holographic System in Water	9
3.	Spectral Attenuation Coefficients for Water	10
4.	Acoustical Pulsing and Synchronizing Circuit	12
5.	Gate Timing Input - Delay Circuit	13
6.	Strain Gage Circuit	16
7.	Hydrophone Circuit	17
8.	System for Making Double Pulsed Holograms in Air	21
9.	Membrane for Measuring Piston Displacement Holographically	23
10.	Acoustic Signal Generation Circuit	29
11.	Continuous Wave Laser Interferometer	32
12.	Photo-diode Circuit	36
13.	Typical Photodiode Output	37
14.	Acoustic Pulse Generation Circuit	40
15.	Acoustic Pressure Sensing Circuit	42
16.	Cylindrical Rod Assembly in Pool (side View)	43
17.	Representation of Oscilloscope Picture of Sampled Waveform	45
18.	Axial Displacement Profiles for 9.8, 19, and 23 KHz	48
19.	Axial Displacement Profile for 29.1 KHz	50
20.	Axial Displacement Profile for 33.4 KHz	51

Figure	Title	Page
21.	Axial Displacement Profile for 47.6 KHz	52
22.	Axial Displacement Profile for 61.5 KHz	54
23.	Axial Displacement Profile for 68.5 KHz	55
24.	Axial Displacement Profile for 85.9 KHz	56
25.	Axial Displacement Profiles Predicted by Mathematical Model	58
26.	Axial Displacement Versus Time for Various Radial Points	60
27.	Second Branch Contribution to Velocity Profile for Various Frequencies	63
28.	Summation of Velocity Branches One and Two for Various Phase Relationships	64
29.	Pressure Distribution for 10.52 KHz	69
30.	Pressure Distribution for 23.02 KHz	70
31.	Pressure Distribution for 30.01 KHz	71
32.	Pressure Distribution for 47.5 KHz	72
33.	Pressure Distribution for 61.5 KHz	73
34.	Pressure Distribution for 87.5 KHz	74
35.	Predicted Radiation Patterns for Rod and Piston for Frequencies 12.5 - 50 KHz	75
36.	Predicted Radiation Patterns for Rod and Piston for Frequencies 62.5 - 87.5 KHz	76

LIST OF PLATES

Plate	Title	Page
1.	Holographic Interferogram of Piston Motion	24
2.	Experimental Arrangement for Displacement Measurements	33
3.	Photo-diode Output for Sinusoidal Input	39

LIST OF TABLES

Table	Title	Page
1.	Inductance Needed to Negate 0.005 Microfarads for Various Frequencies	30

CHAPTER I

INTRODUCTION

A. Statement of the Problem

The problem of a semi-infinite cylindrical, elastic rod propagating longitudinal stress waves, set in an infinite baffle and radiating from its end into a semi-infinite, liquid, non-viscous medium has been experimentally investigated. This investigation was concerned with measurement of pressure fields in water and measurement of the radial distribution of axial particle displacement on the radiating face. These measurements are of interest and importance because in calculating the pressure field generated by a vibrating boundary such as a transducer face one must know or assume the velocity profile of the vibrating surface. In most cases,[1,2] to facilitate computations, the vibrating surface is assumed to vibrate as a plane. In typical calculations for power, beam pattern, etc. this assumption served as a fairly accurate model for the true physical situation only so long as $ka << 1$, where k is the propagation constant ω/c and a is the rod radius. This condition corresponds to a small transducer radius, and low frequency. For small ka however, the real part of radiation impedance, and thus radiated power, is low so that one desires to operate at values of ka for which the plane piston approximation is invalid.

A number of recent papers have been published with theoretical calculations of velocity profile on the end of an elastic cylinder.[3,4] Maxwell[5] has theoretically solved for velocity profiles on the end of an elastic rod and the radiated pressure distribution in a fluid. To the knowledge of the author measurements of velocity profiles and resulting radiation patterns as functions of

frequency, by which theoretical models can be checked, have not previously been made. This dissertation discusses measurement methods, describes the methods used and presents measured velocity profiles on the end of a long aluminum rod and the resulting pressure radiation patterns in water.

B. Historical Background

Early work done in the area of vibrations of an elastic circular cylinder was done by Pockhammer[6] and Love[7]. In 1947 Davies[8] published an extensive study of the "Hopkinson Pressure Bar". In this study some experimental work was done to measure axial displacement of the rod end as a function of time rather than as a function of radial position. The non-uniform displacement distribution over the radius was known as a source of error in Davies measurements since he was using a capacitive device to measure the average displacement of the rod end with time. Kolsky[9], in his book, discussed a number of experimental investigations. These were concerned with determination of the velocities of propagation of elastic waves in a rod (dispersion curves) dynamic measurement of stress-strain relationships, and measurement of other elastic properties of materials. Apparently no attempt was made to determine axial displacement profiles on the end of a rod. Volterra and Zachmanoglow[10] also discuss wave propagation in elastic solids, but again they study elastic properties of a rod such as dynamic yield stress, velocity of wave propagation and dynamic stress strain relationships. A good bibliography of others who have contributed to similar studies is listed by Volterra and Zachmanoglow. Zemanek did considerable work, both theoretical and experimental, on the cylindrical rod problem. Using an approximate solution made up of the first nine of the infinite

eigen-values of Pockhammer's frequency equation a computer solution was generated to yield dispersion curves, distribution of stresses, and axial and radial displacement distributions. Experimentally, a resonance method was used to measure dispersion and the standing wave pattern along the length of a rod. A measurement of axial displacement across the end of the rod was also made as a method of identifying the mode of propagation only. No measurement of velocity profile variations as a function of frequency or associated radiated beam patterns was reported. Miller expanded on the work of Zemanek by assuming a semi-infinite cylindrical rod propagating into a semi-infinite cylindrical column of water. Displacement and stress fields in the rod were expressed as an infinite sum of eigen-values relating to the infininte solutions of Pockhammer's equation with appropriate boundary conditions applied. By truncating the solution to the sum of thirty-one branches and forcing the boundary conditions to hold at a finite number of points on the rod/water interface the fields in the rod and in the water as well as the axial displacement distributions were calculable by computer. Measurements of velocity profiles and radiation patterns, by which this mathematical model could be checked, were not made.

In 1970 Maxwell expanded on Miller's work by allowing the rod to couple to a semi-infinite fluid rather than a cylindrically bounded one. Using the same techniques as Miller, computations were made to determine axial distribution of velocity on the interface, reflection coefficients and radiated pressure distribution in the water. No experimentation was involved in this work.

C. Format of the paper

This chapter provides an introduction to the report, a definition of the problem, and a brief historical summary of work done which relates to this project. Chapter II discusses the optimum experimental method, limitations imposed by the physical system and by available equipment and the evolution of the experimental method due to these limitations.

Chapter III describes in detail the final experimental method used to take measurements. Results of the experiments are given in Chapter IV. These results are discussed and are compared with existing theory in the same chapter.

Conclusions and recommendations of areas for fruitful further research are provided in Chapter V.

CHAPTER II

EVOLUTION OF THE EXPERIMENTAL METHOD

A. The Optimum Experiment

In developing this experiment the original intent was to establish physical conditions which would closely match the assumed conditions of Maxwell. This would provide data to check the accuracy of the theoretical model. Although the experimental procedure could not attain the ideal conditions assumed by the theory, the discussion will start by assuming that the conditions can be met and will develop into the final workable experiment as limitations are imposed and approximations are made.

For his theoretical study, Maxwell assumed a semi-infinite, cylindrical, aluminum rod whose radiating end was in the plane of an infinite baffle and radiating into a semi-infinite body of water. All other surfaces of the rod were assumed to be exposed to vacuum.

The optimum experiment to match the above conditions was designed as follows: An aluminum rod is positioned inside a metal tubular housing. The back of the housing is sealed with a plate, but has a watertight connector in the center to allow passage of power supply and instrumentation wiring. The front end of the housing is closed to nearly the rod diameter so that when the aluminum rod is in place, an O-ring seal will prevent the entry of water into the housing (See Fig. 1). Thus the only portion of the rod in contact with water is the radiating face. The air boundary around the solid rod approximated a free surface as assumed by Maxwell since the characteristic impedance of aluminum is four orders of magnitude greater than the characteristic impedance of air.[11]

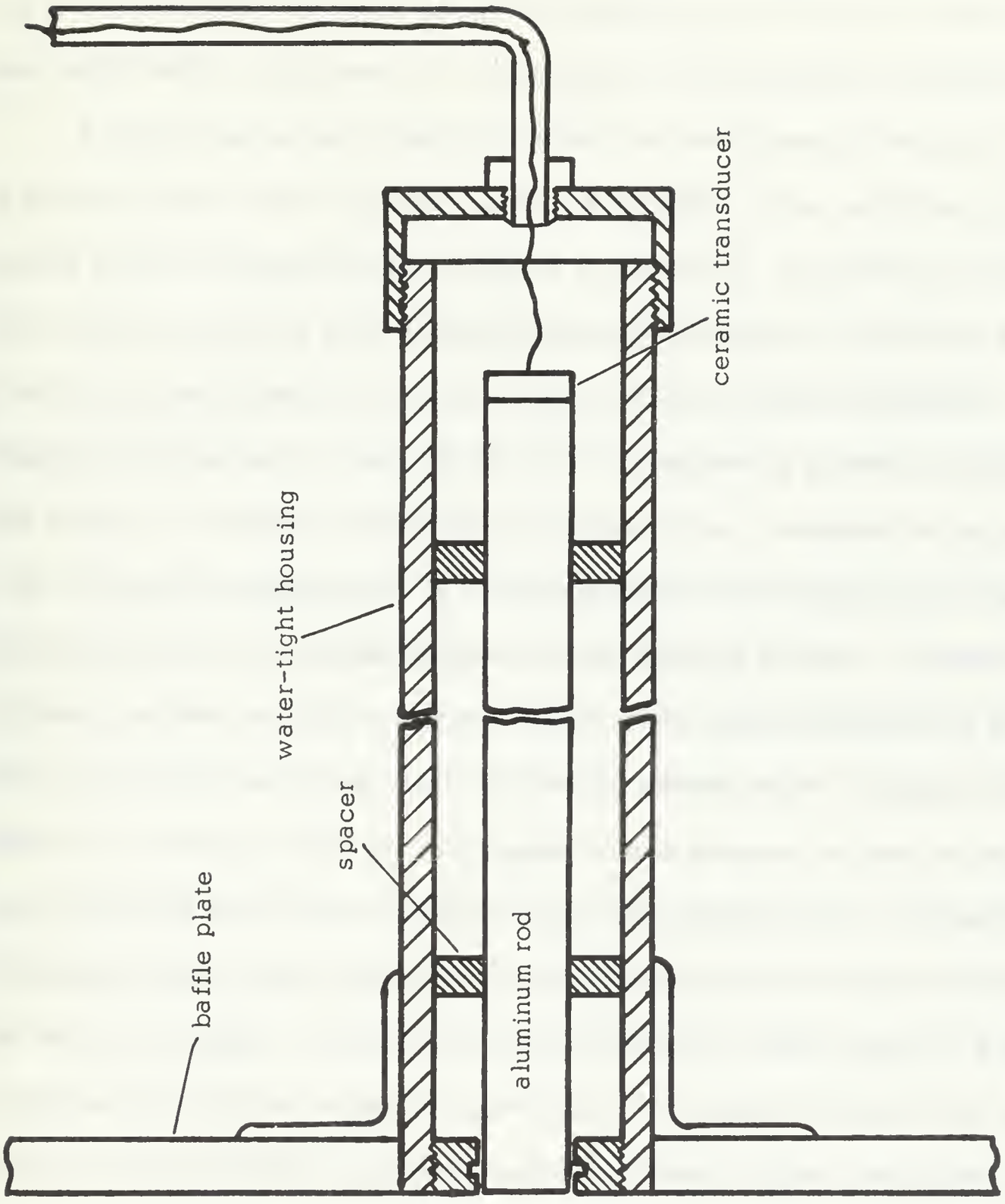

Fig. 1 Vibrating Rod and Housing Assembly

In order to approximate the infinite baffle assumption the cylindrical housing for the solid rod is connected to a large metal plate. The baffle can be finite in size if the reflections do not return to the vibrating rod face from the end of the finite baffle while measurements are being taken. This requires a pulsed signal.

A hole in the center of the plate allows the positioning of the rod so that its vibrating face is flush with the surface of the baffle. The solid rod in its housing is then suspended in the middle of a large pool. To satisfy the infinite baffle condition and free field acoustic condition the system is driven by a pulsed sinusoidal potential activating a piezo-electric driving transducer mounted to the free end of the solid rod. The transducer is a ceramic (Clevite, 5400 series), 1.5 inches in diameter by 0.22 inch thick. Attached to the surface of the rod near the radiating end is a semi-conductor strain gage for the measurement of the stress wave packet incident on the radiating rod face. Standard hydrophones can then be used to measure the far-field radiated pressure in the water. It was planned to use laser holographic interferometry to measure the motion of the vibrating rod end. A holographic interferogram is made by exposing a high resolution film plate to coherent laser light reflected from a moving object. Two exposures are made in which this light is combined with reference laser light in the film plane. Development of the holographic plate results in a pattern of light and dark fringes caused by interference of the light reflected from the rod end at its two different exposure positions. These fringes correspond to loci of equal displacement from the rest position.

Quantitatively,

$$I_{image} = I_o[\, J_o(2\pi d/\lambda_\ell)\, (\cos\alpha + \cos\beta)]^2 \quad [12] \quad \text{where,}$$

α = illuminating angle

β = viewing angle

d = displacement of a point on the rod

I_o = intensity for no motion

λ_ℓ = light wavelength.

As an example one sees that dark fringes occur whenever, $d = (\lambda_\ell/2\pi)A_n$, where the A_n are zero arguments for the zero order Bessel function. Thus each holographic interferogram is a quantitative representation of the position of every point on the rod end at the instant of sampling.

If the developed photographic plate is returned to its original position and illuminated by the reference beam an image of the vibrating surface with the interference fringes on it will appear. This image can be photographed by conventional means and pertinent displacement data can be taken from the photograph.

The holographic system required consists of a high power pulsed laser, a reference reflector and holographic film plates as shown in Fig. 2. The laser must have a pulse duration much shorter than the period of the acoustic wave (0.1-0.01 millisecond). A large peak power output is required to provide sufficient energy to expose properly the holographic film plates during an extremely short exposure time. A currently available laser which would be optimum has a light wavelength of 0.53 micron. This wavelength is in the region of minimum attenuation in water as shown in Fig. 3.[13] The entire holographic

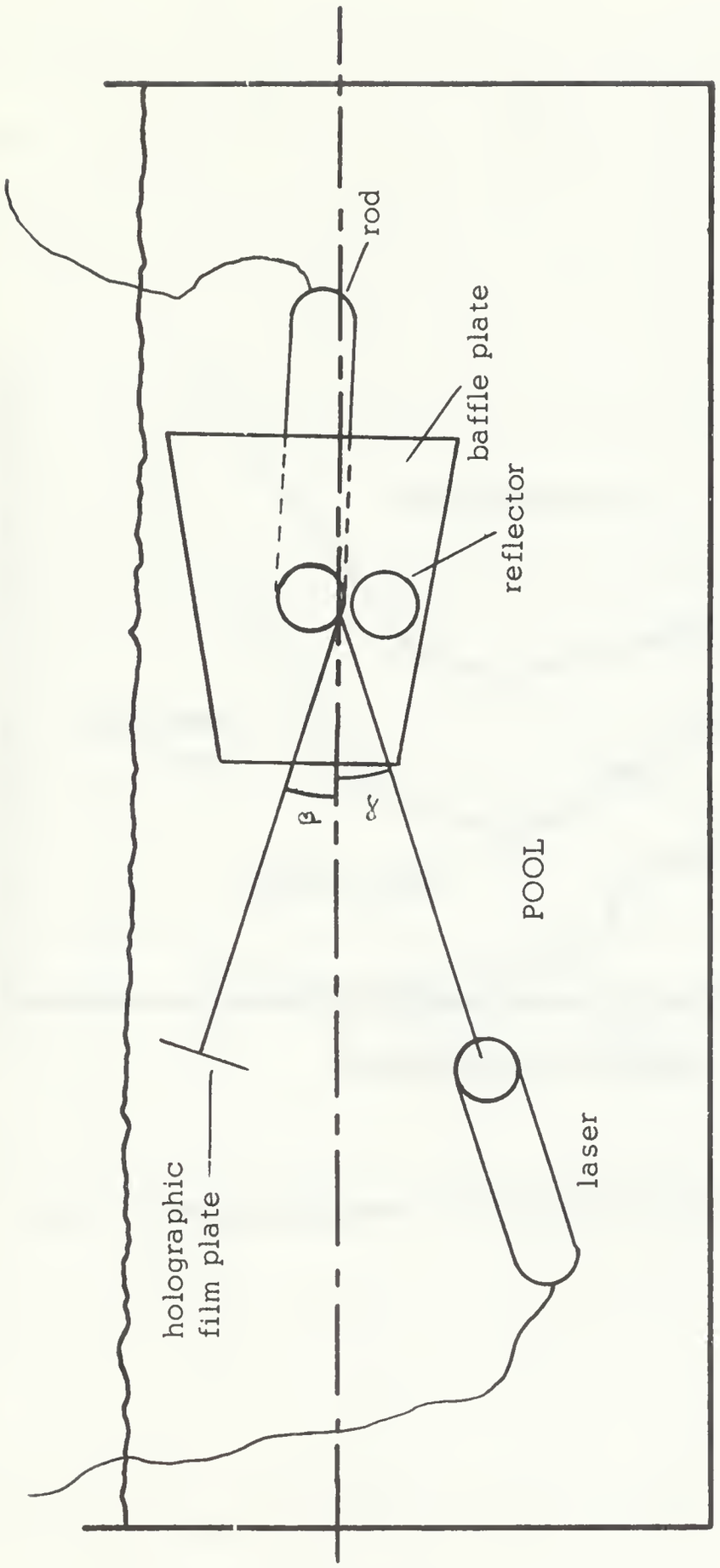

Fig. 2 Holographic System In Water

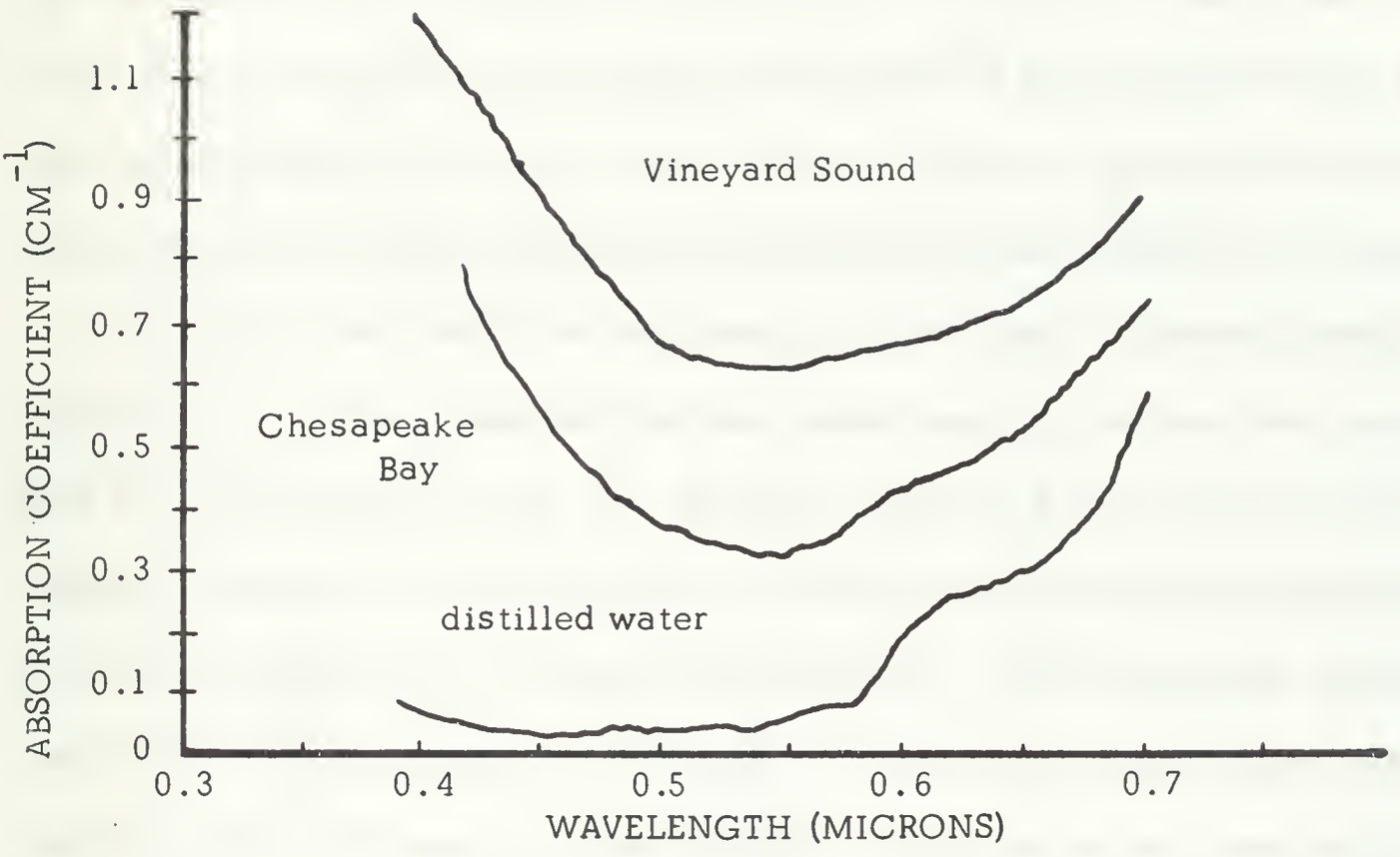

Fig. 3 Spectral Attenuation Coefficients for Water

system is submerged to eliminate refraction problems at the air/water interface.

The piezo-electric transducer on the end of the solid rod is driven by a pulsed sinusoidal wave-packet. As shown in Fig. 4 the wave packet is formed with a tone burst generator. The tone burst generator is capable of gating from 1 to 128 cycles of an input oscillator signal. The tone burst is completely coherent in that it always begins at exactly the same phase. Therefore, the spectral content of the signal to the transducer is completely repeatable. Out of the tone burst generator the signal is amplified and then passed through a step-up transformer to raise the signal voltage. The high voltage (about 600V, peak to peak) tone burst at the desired frequency is then passed to the transducer.

Timing of the tone burst and emission of the laser is accomplished by initiating a laser fire trigger and the gate timing input to the tone burst generator with the same signal (See Fig. 4). However, due to a delay in the laser fire system a continuously variable delay is inserted into the initiating signal going to the gate timing input of the tone burst generator. The continuously variable time delay is accomplished, as in Fig. 5, by generating a square pulse with variable pulse width using a pulse generator. The pulse is then sent through a differentiator whose output is then spikes corresponding to the leading and trailing edges of the square wave. A clipping circuit (diode) is then used to pass only the negative going spikes which correspond to the trailing edge of the square pulse. Thus when the system is initiated, a signal goes immediately to the laser fire trigger and to the input of the pulse generator. After some delay, controlled by varying pulse width, a voltage spike initiates the gate timing input of the tone burst generator. By adjusting this delay circuit the laser

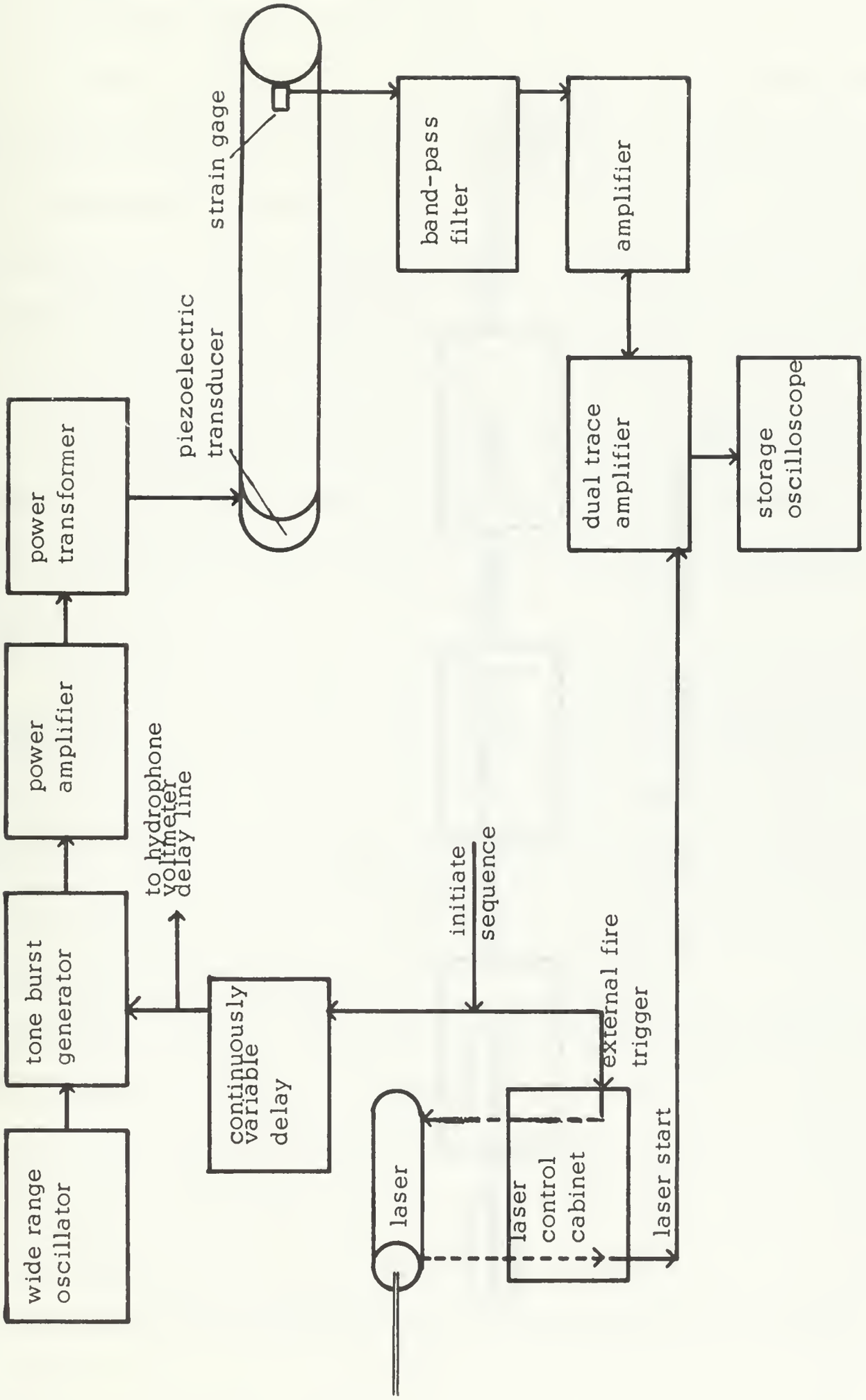

Fig. 4 Acoustic Pulsing and Synchronizing Circuit

Fig. 5 Gate Timing Input - Delay Circuit

emission can be synchronized to the arrival of any portion of the acoustic signal at the rod/water interface. Since it takes about 0.70 millisecond for the acoustic signal to travel the length of the rod, a delay of about 11.3 milliseconds will be required to synchronize the acoustic signal with the laser emission which is internally delayed by about 12 milliseconds. The purpose of this timing is not an accurate measurement of which portion of the acoustic signal has been photographed with the laser. This timing merely allows rough control sufficient to insure that laser emission will occur during some portion of the acoustic signal time. The degree of this control will depend upon the amount of jitter in the laser fire delay. The precise measurement of which portion of the acoustic wave packet has been sampled at the face of the vibrating rod will be discussed later.

The length of the signal wave-packet is limited by the infinite-rod, infinite-medium approximation. It is necessary that the duration of the wave packet be less than the time of travel down the cylindrical rod (about 0.73 millisecond). Thus for reflection coefficient measurements, if the strain gage is located at the lengthwise center of the rod the trailing edge of the transmitted signal will pass the strain gage before the leading edge of the reflected wave arrives there. This will enable accurate comparison of the incident wave with the reflected wave. This restriction on wave-packet length allows wave-packets of from seven to seventy cycles for frequencies ranging from 10 KHz to 100 KHz. The period of one cycle in the wave-train will vary from 0.1 to 0.01 millisecond for the specified frequency range. Use of a 10 nanosecond pulse to sample rod motion will allow at least a thousand distinct samples to be taken over the

period of the oscillation. Hence the assumption that instantaneous point samples are to be taken is valid.

A strain gage is mounted near the radiating end of the cylindrical rod. It is a low resistance, semi-conductor type by Baldwin-Lima-Hamilton and has an active length of 0.2 inches. Output of the strain gage will, to experimental tolerance, specify the acoustic signal at the rod end. This is compared with the laser emission time to determine which spot on a cycle of the wave train has been sampled. Circuitry for the strain gage as shown in Fig. 6 consists of a 50 volt, d-c source supplying an approximately constant current to the strain gage through a 2.0 KΩ resistor. Resistance of the strain gage changes as the strain changes causing voltage fluctuations which are amplified and displayed on the face of an oscilloscope.

For measurement of acoustic pressure in the far field of the radiating rod a standard hydrophone (Atlantic LC-10, 10-100 KHz) is used. Fig. 7 shows that the output of the hydrophone is filtered to eliminate noise and then displayed on the face of an oscilloscope. In addition, the hydrophone output is fed to a gated, sample and hold type voltmeter. The voltmeter is gated through a continuously variable delay circuit (same as Fig. 5). Adjusting the time and duration of gating will cause the voltmeter to read only the steady-state portion of the voltage wave-packet received from the hydrophone. This enables maximum accuracy of pressure measurements. Location of the hydrophone is varied over the farfield to obtain an accurate description of the pressure directivity pattern. The hydrophone must be kept far enough from the source to insure that reflections will not reach the source before holographic sampling is complete.

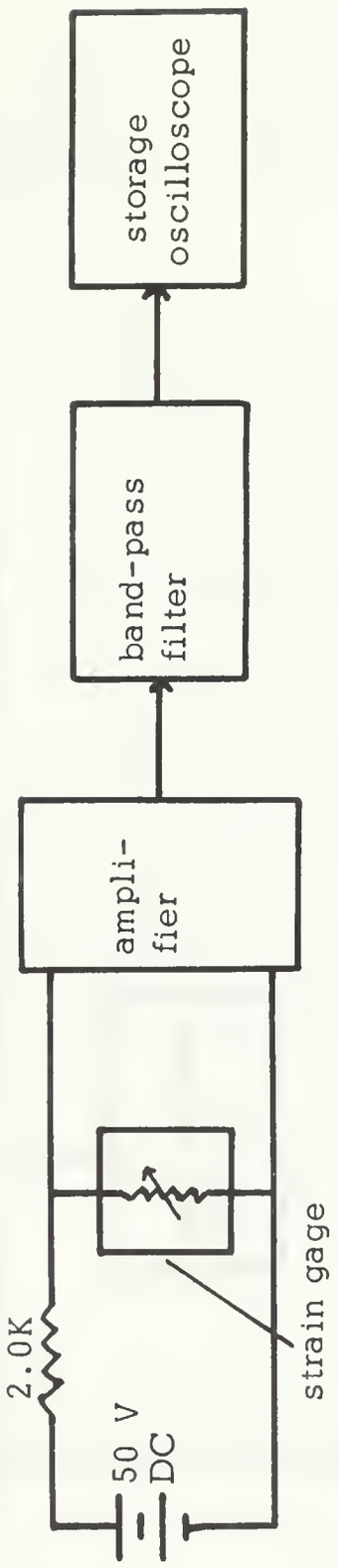

Fig. 6 Strain Gage Circuit

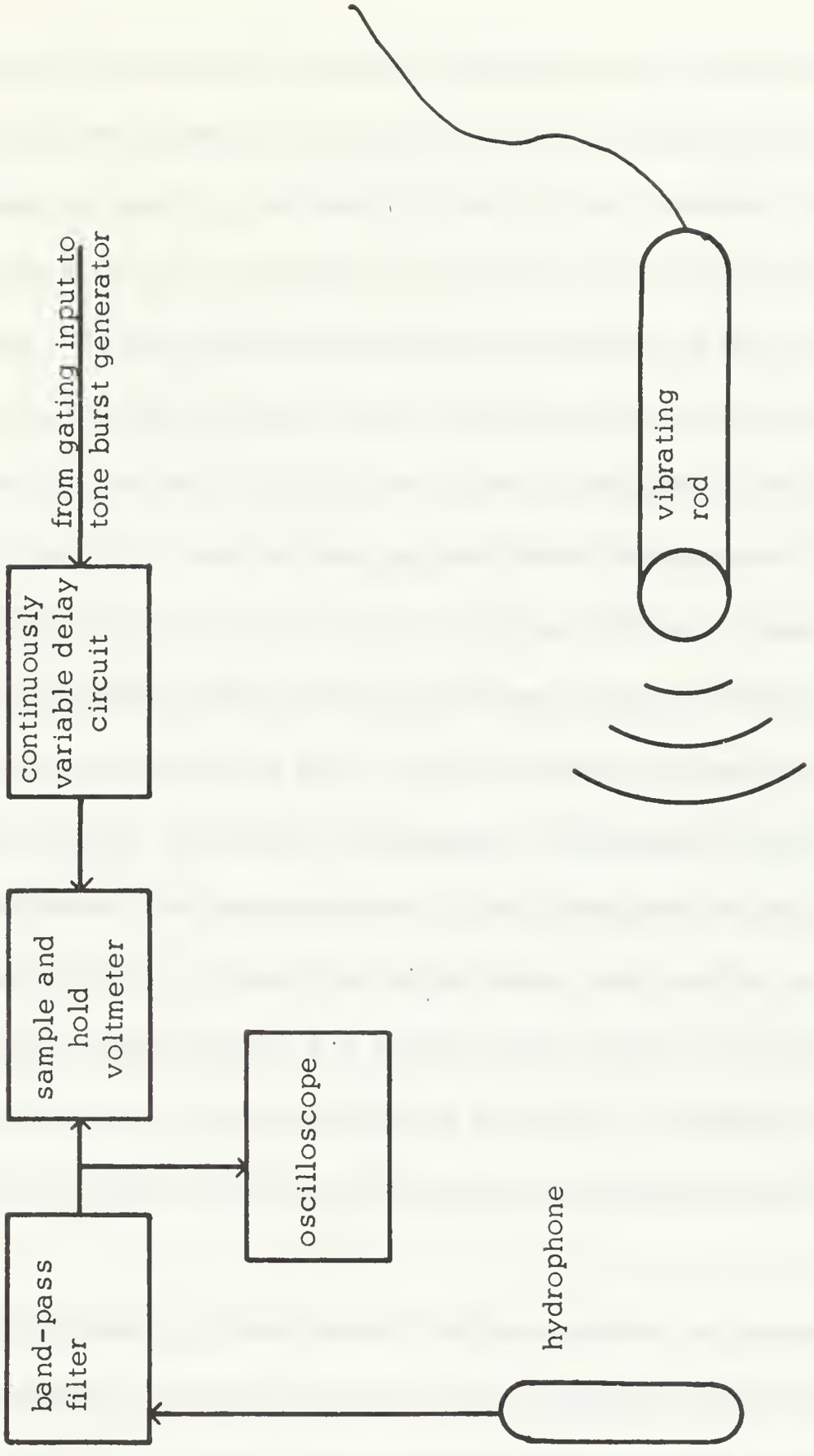

Fig. 7 Hydrophone Circuit

The set-up for recording holographic interferograms is rather simple (See Fig. 2). With the vibrating rod in its encasement centered three feet below the water surface the laser is positioned so that its front window is two feet below the rod end with the longitudinal axis pointing to the lowest point on the vibrating surface. This allows for the smallest divergence of the laser beam to illuminate both the vibrating surface and a reference mirror attached to the rigid baffle just below the rod end. A film plate holder is mounted in the water at a depth of one foot with its plane surface perpendicular to the axis of a laser beam specularly reflected from the bottom of the vibrating rod face. Emersing the entire apparatus minimizes difficulties of refraction at the air/water interface. Geometry of the set-up minimizes path length differences between the reference and object beams for the holographic exposures. Experimental work by Varnado and LaGrone* indicates that laser radiation in the blue-green region loses none of its spatial coherence by propagation through water path lengths of up to 12.5 attenuation lengths (approximately 2.5 meters for tap water). All parts of the holographic apparatus must also be stationed at least 0.75 meter from the radiating surface to prevent acoustic reflections from interfering with the measurements.

For each frequency studied several double exposure holographic interferograms are required to describe accurately the instantaneous time displacement profile of the vibrating rod over at least one steady-state cycle of motion. After placing a film plate in the holder, the laser is pulsed one time with the rod

---

*Varnado and LaGrone, op. cit., p. 2.

stationary. A second exposure is then controlled to occur at a certain point on the wave-train by using the simultaneous laser fire and delay line actuation to the tone burst generator described earlier. After the laser fire/acoustic pulse sequence has been initiated a precise measurement of which portion of the wave-packet has been sampled is determined as follows: Refer to Figure 4. Using a trigger output from the underwater laser which coincides with laser emission and the strain gage mounted near the end of the radiating rod a dual trace storage oscilloscope in the "ADD" mode will display a picture of the acoustic wave-packet with a spike, corresponding to laser emission, superimposed. One can directly read which spot on the wave-train was sampled by the laser. These data are recorded with an oscilloscope camera.

Once the second exposure has been made and its position on the wave-train recorded the sample is complete. Varying the delay of the tone burst generation allows for sampling over the entire wave-packet.

B. Experiment Modifications Dictated by Physics and Facilities

For several reasons the experimental procedure just described had to be modified for this work. First, an underwater laser was obtained.* This equipment was a Neodimium doped YAG laser with a frequency doubler (KDP crystal) to provide light at 0.53 micron. The unit could be controlled to provide from one to sixty pulses per second with a pulse width of seven nanoseconds and power level of 500 kilowatts. Although this would be the ideal light source it could not be employed for holographic work due to extremely short coherence length. Unavailability of other underwater pulsed lasers dictated the measurement

*Union Carbide Corp., Korad Div., Underwater Laser System.

of displacement profiles in air. Computer analysis of the theoretical calculations for axial velocity profiles indicated that little difference in profiles should be expected between the aluminum/air and aluminum/water situations over the frequency range of interest.

Extensive work was done in an effort to take pulsed holograms with the pulsed acoustic wave passing the rod/air interface. The use of a pulsed ruby laser with pulse width of thirty nanoseconds and one joule output at 6943 angstroms was obtained†. This laser was equipped with a dye-cell Q-switch. Changing dye concentration permitted one to control the laser output to a single pulse or to two pulses spaced about fifty microseconds apart. Although the spacing between pulses could not be controlled, by double pulsing the laser while the acoustic wave was on the rod end a holographic interferogram was produced. Fig. 8 shows the physical system for making the double-pulsed holograms in air. The acoustical and synchronizing circuits remained as previously described. The interference rings on the hologram correspond to displacement of the rod over the fifty microsecond interval between laser pulses. Coherence length of this laser was estimated at thirty feet!

It must be noted at this point that if the object under study is moving as a plane piston then a double-exposure hologram will not show interference rings. Since all points on the face move the same distance over the interval between pulses the interferogram will be entirely one shade of gray corresponding to the phase interference between the reflections from two planes at the instants

---

†Hadron, Inc. Pulsed Ruby Laser System.

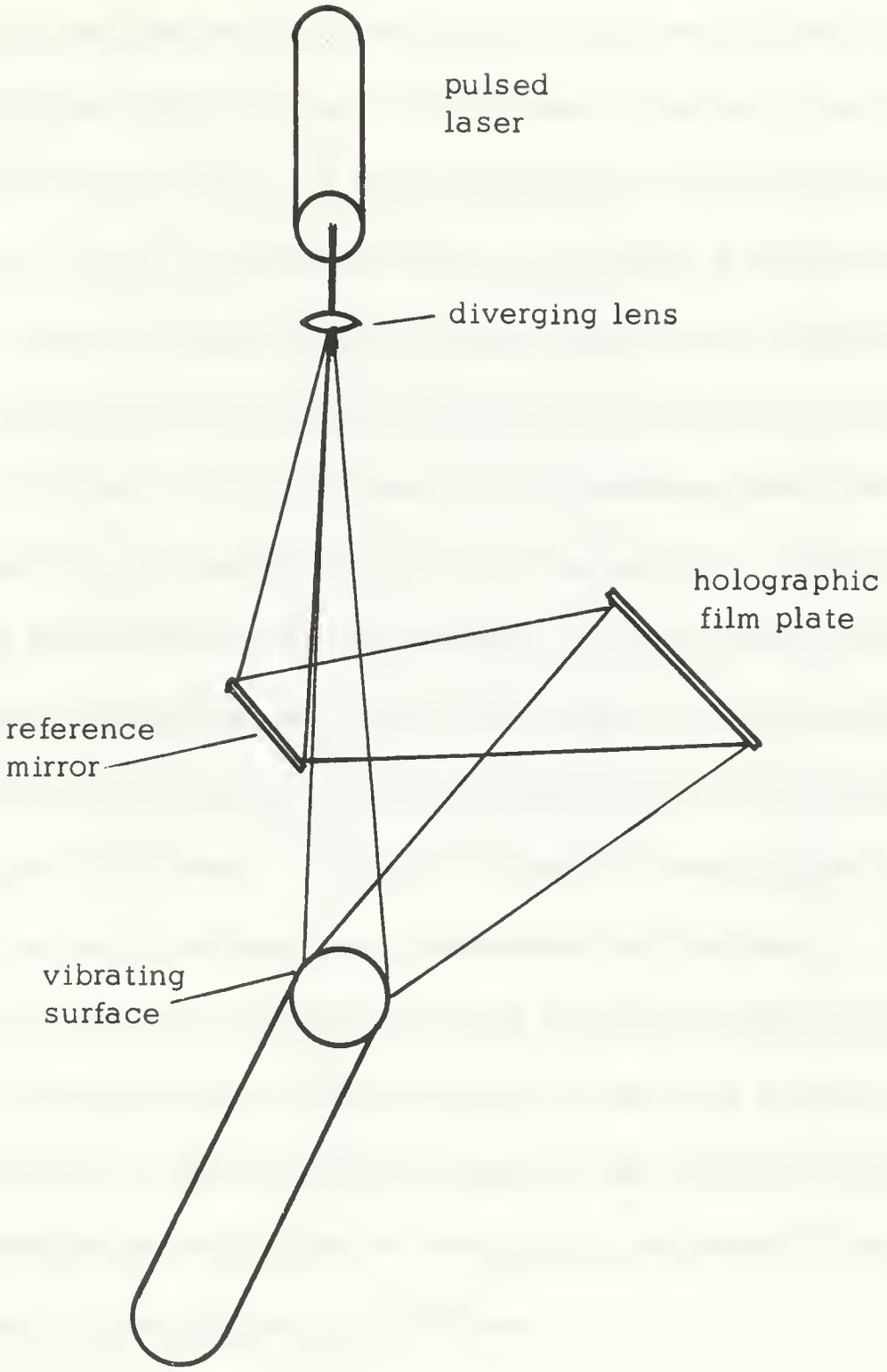

Fig. 8 System for Making Double
Pulsed Holograms in Air

of pulsing. This situation closely corresponds to the expected motion at the lower end of the frequency spectrum studied. An attempt was made to measure this approximate plane motion by stretching a rubber membrane across the rod end. Fig. 9 shows that the membrane was glued to the rod face and to the baffle plate at a radius of four inches. Now instead of having a step change in displacement at the rod radius the displacement is a linear function of radius from the rod edge to the membrane edge. By making a double-exposure hologram of the entire membrane area interference rings can be obtained; the total number of interference rings corresponding to the plane piston like displacement of the rod end. Holograms taken of the membrane (See Plate 1) verified the piston-like rod motion for the lower frequencies. Quantitative measurements of displacement were inconsistent, however; due to the likelihood that the membrane displacement was not actually linear with radial position. It is felt that rather than being linear the edgewise profile of the membrane with rod motion was oscillatory. Figures 10.b and 10.c would imply identical interferograms, but would indicate true displacement only in case b. Time limitations on use of the laser system precluded extensive study of other possible means for determination of displacement in the case of piston motion. For higher frequencies holographic interferograms of the membrane did show at least one interference ring within the rod radius thus qualitatively confirming that motion of the rod face ceases to be uniform.

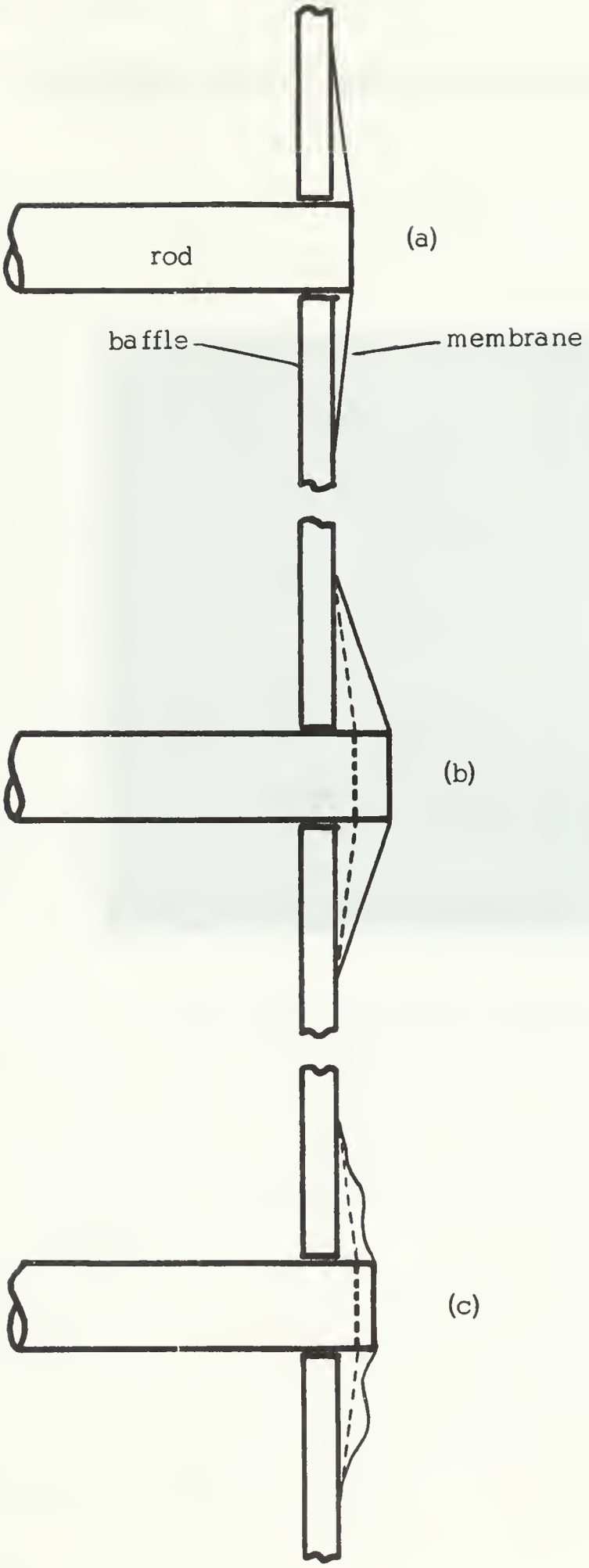

Fig. 9 Membrane for Measureing Piston Displacement Holographically

PLATE I

Holographic Interferogram of Piston Motion

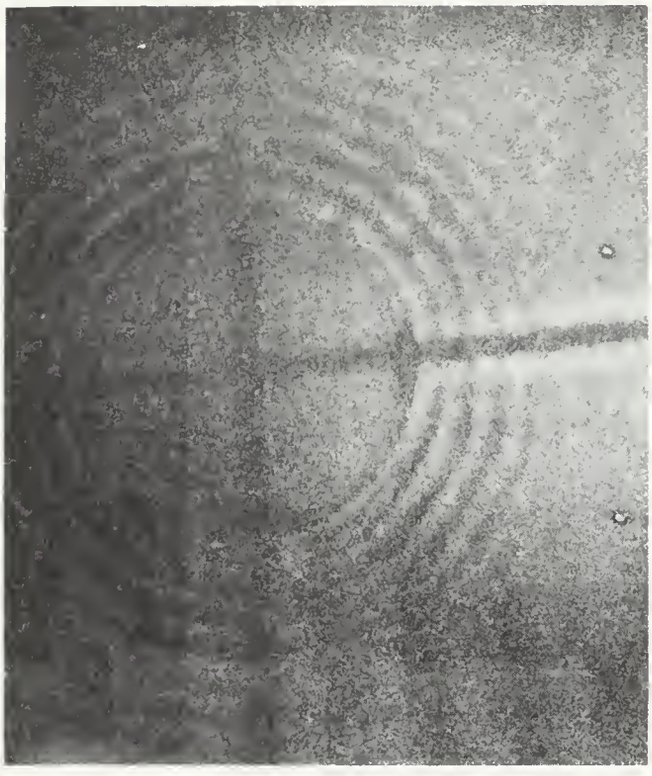

Accurate measurement of the displacement profile becomes increasingly difficult with higher frequencies. This can be seen by expressing the particle velocity as,

$v = F/\rho CA$ where,

F = force

ρ = density of the rod

C = speed of propagation in the rod

A = cross-sectional area of the rod.

Displacement is found by taking the time integral of velocity which, for the case of a harmonic velocity function, simply becomes, $x = \frac{v}{j\omega} = F/j\omega\rho A$, where ω is the radian frequency. Thus, an increase in frequency reduces the realizable displacement. The inability of currently available power sources to boost the signal to a large undistorted pulsed voltage at high frequency resulted in such small motion that accurate displacement measurements were impossible with this system. It was decided to excite the rod with a continuous-wave signal tuned to a longitudinal resonance of the rod. In this way it was felt that perhaps the pulsed laser holography might yet prove to be fruitful. Lack of sufficient displacement for accurate interferograms even by the resonance method demanded a final alteration of the measurement technique used to gather displacement data.

C. Final Test Method Used

Having determined that available distortion-free power, transducer characteristics and frequency limited rod end displacements to near one wavelength of laser light, a measurement system was adapted which enabled accurate determination of this small motion. The method adapted involves use of a modified Twyman-Green interferometer as described by Monahan and Bromley*. This method permits measurement of displacement down to one-half wavelength of the laser light used in the interferometer. Rather than obtaining an entire displacement pattern for the rod face as in a holographic interferogram this method involves point sampling. Thus, assuming that displacement of the rod is symmetrical about the axial centerline a series of point samples taken along a radius of the rod will provide the required displacement profile. A complete and detailed description of the experimental system is described in the following chapter.

---

* Monahan and Bromley, op. cit., p. 24.

CHAPTER III

THE EXPERIMENT

A. Measurement of Displacement Profiles

The experimental situation which evolved from the optimum because of physical and equipment limitations was as follows. Perform the displacement measurements in air since no adequate underwater laser is available. Generate the largest distortion free continuous-wave electric signal possible. The use of a continuous-wave signal for measurement of displacement profiles did not invalidate the infinite baffle, semi-infinite medium approximation since the measurement was made in air. This becomes quite evident when one considers, again, the vast mis-match between the characteristic impedances of aluminum and air. Any reflected signal in the air returning to the radiating rod face would certainly have an immeasurably small effect on its motion. Likewise the semi-infinite rod approximation was not jeopardized by the use of a continuous-wave signal. This is true because the rod is much longer (96 times) than its diameter, and only the lowest mode would propagate for the frequency range employed.* Higher order modes generated on reflection from one end could not propagate the length of the rod to disturb the motion of the opposite end. Thus the continuous-wave signal at the rod end was the same as that part of the pulsed signal which reached the rod end, except that, being at a longitudinal resonance frequency, the continuous-wave signal induced larger motion.

Tune the continuous-wave signal to various longitudinal resonances of the aluminum rod over the frequency range 10-100 KHz as determined by the

---

* Op cit, Zemanek, pp. 19.

resonance equation, $f = nc/2\ell$, where

n = an integer

c = velocity of propagation

ℓ = length of rod.

Take axial displacement measurements at these frequencies using a modified Twyman-Green interferometer employing a continuous wave Helium-Neon laser as the light source. For each frequency take several point measurements along a rod radius to establish the axial displacement profile.

Use of a continuous-wave signal to excite the rod greatly simplified the acoustic signal generation circuit (See Fig. 10). A wide range oscillator (Hewlett-Packard, Model 2000-A) provided the basic sinusoidal signal over the full range of frequencies investigated. Accurate frequency indication was provided by an electronic counter (Hewlett-Packard, Model 5221-A). The sinusoidal output from the oscillator was first amplified by a wide band, 10 watt, amplifier (Krohn-Hite, Model DCA-10R) to provide a maximum input signal to a large wide band, 50 watt amplifier (Krohn-Hite, Model DCA-50R). Output of the amplifier was sent through a matching transformer. Finally the signal was sent to a series connected combination of the ceramic disk and a variable inductance coil. The function of the coil was to cancel out the capacitive reactance of the ceramic transducer and maximize the real power going to the rod. The measured capacity of the ceramic was 0.0050 microfarads. Table 1 indicates the required series inductance to negate the ceramic capacitance over the range of frequencies studied. At each frequency measured output of the signal generating circuit was set to just below that value for which distortion began to appear on an oscilloscope trace of the signal.

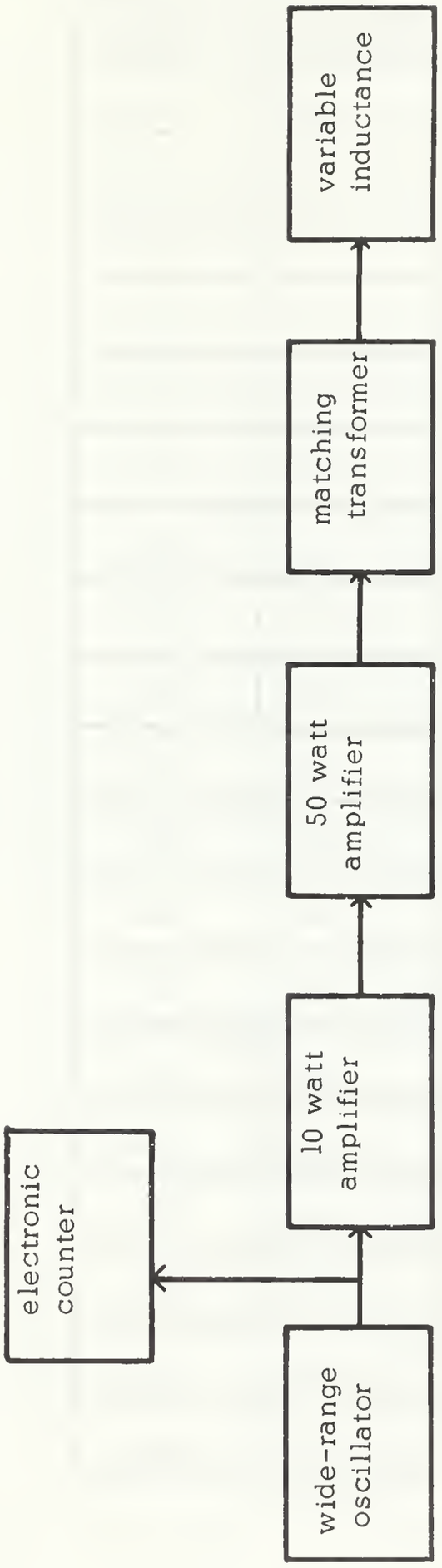

Fig. 10 Acoustic Signal Generation Circuit

Frequency (KHz)	Inductance (millihenry)
10	50
15	20
20	11
25	8
30	6
35	3.5
40	3.1
45	2.2
50	2.0
55	1.5
60	1.4
65	1.2
70	1.0
75	0.9
80	0.8
85	0.7
90	0.6
95	0.55
100	0.5

Table 1. Inductance Needed to Negate 0.005 Microfarads for Various Frequencies

Use of a continuous-wave interferometer necessitates the employment of a stable platform to isolate the experiment from external sources of motion such as building vibrations. For this work a platform was built on a concrete floor of the basement located in the Underwater Acoustic Laboratory Facility at the University of Texas. The platform consisted of a wooden box six feet wide and twelve feet long resting on twelve partially filled twelve inch diameter inner-tubes. The box was filled with approximately 4500 pounds of washed sand. A working surface was established by laying a five foot by eleven foot plate of cold rolled steel weighing about 1200 pounds on the sand surface.

The experimental apparatus placed upon the stable platform consisted of the aluminum rod, a Helium-Neon laser, various lenses and mirrors making up the interferometer, and a photo-diode (Refer to Fig. 11). Plate II is a phogograph of the displacement experiment as it was set up in the laboratory. All optical components were mounted on heavy, interferometrically stable mounts. The cylindrical rod was supported by two wooden stands with foam rubber wrapping around the rod at the points of support to eliminate inaccuracies due to reflections which could occur with rigid coupling of rod to support. The laser used was a fifty milliwatt, continuous-wave, Helium-Neon system (Spectra-Physics, Model 125). Coherent light at a wavelength of 6328 angstroms was taken from the laser to a microscope objective lens by way of a first surface mirror, M1. The expanding beam was then passed through a double lens system causing it to converge with a focal length of approximately four feet. The slowly converging light was then split into two beams, normal to each other, with a cube-type beam-splitter. One beam was used to illuminate the interferometer

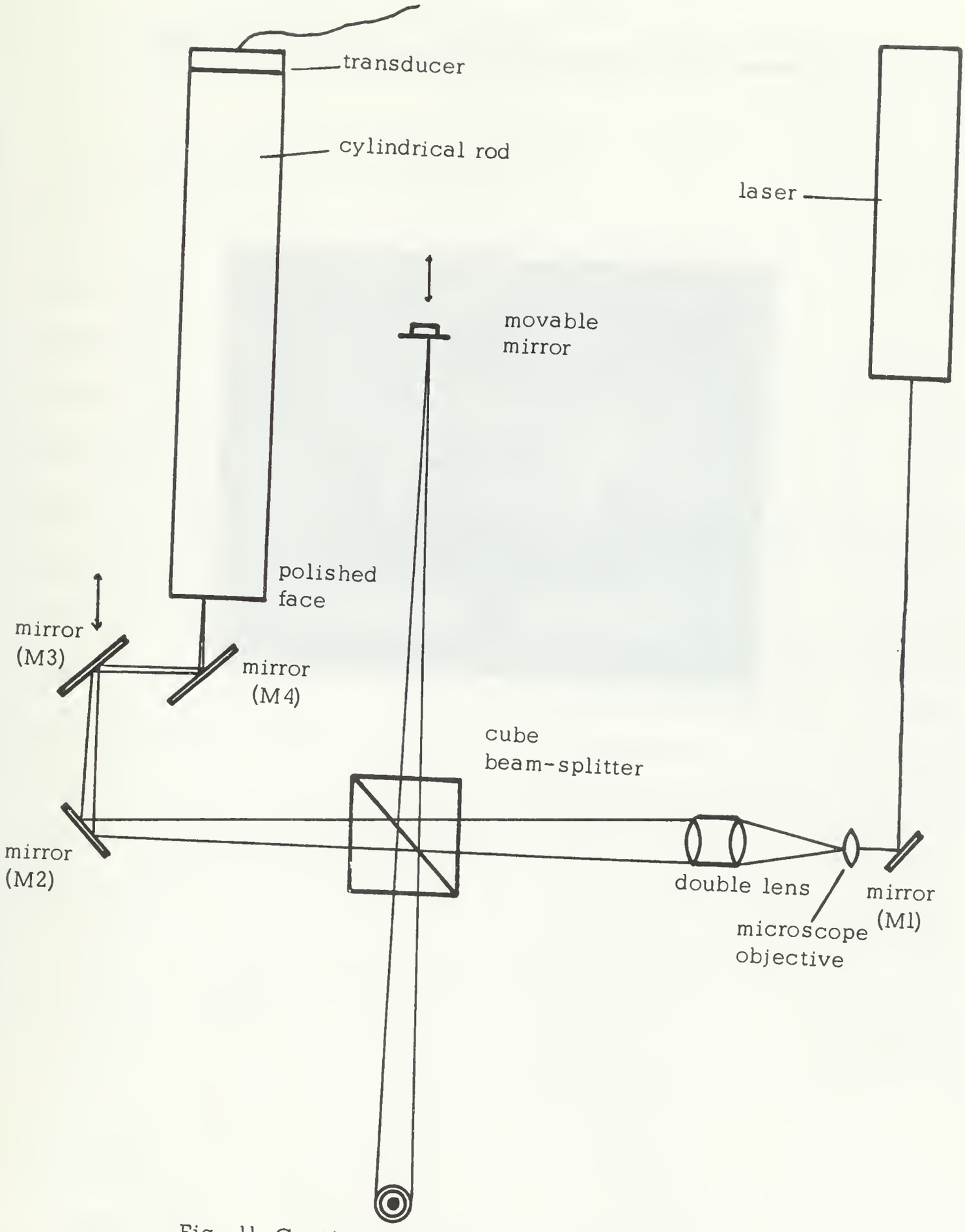

Fig. 11 Continuous Wave Laser Interferometer

PLATE II

Experimental Arrangement for Displacement Measurements

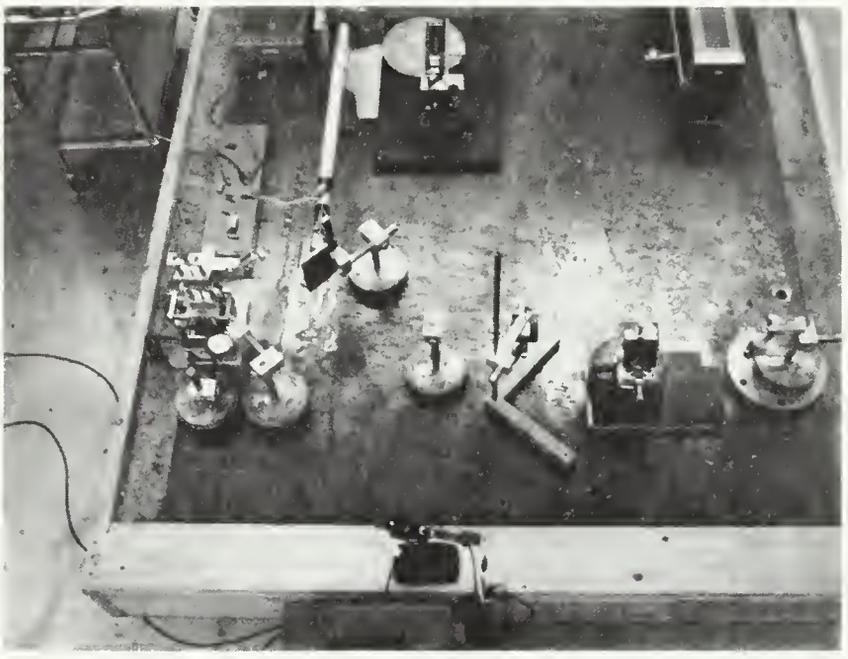

reference mirror which could be positioned so that the plane of the mirrored surface coincided with the focal point of the laser beam. The plane of the reference mirror was perpendicular to the beam axis so that the reflected beam returned back to the beam splitter. The second of the two split beams was used to illuminate the object (rod face) by way of mirrors M2, M3, and M4. These mirrors allowed for path length variation to get the focal point of the beam on the rod face. Additionally mirror M3 was mounted on a translation stage which enabled movement of the sampling point along a horizontal radius of the rod. Relative position of the sampled point was provided by mounting a dial indicator such that is probe was moved by movement of the the translation stage. To provide a highly reflective surface on the rod end it was polished with commercial diamond paste with one quarter micron grit size. Mirrors M2, M3, and M4 also had to be positioned so that the reflection from the rod face returned to the beam splitter. At the beam splitter the two beams, which return diverging, combine and exit to form an interference pattern on a screen placed in the path. This interference pattern is circular in nature, the circular rings representing loci of equal path length difference between rays of the two beams. If the sampling point on the rod face is displaced axially the light path length is changed and one can see the rings of the interference pattern alternately shift from light to dark to light. Each time a circular ring goes from light to dark to light the path length has changed by one wavelength of the laser light, in this case 0.6328 micron. Since the path length change is equal to twice the displacement of the sampled point one cycle of intensity change in the circular ring pattern actually represents one-half wavelength of motion (0.316 micron). Of course, when the

rod face is moving in and out at 10 KHz one cannot see the cyclical changes in the interference pattern. In fact, with rapid motion of the rod face the interference pattern washes out to the appearance of a uniformly illuminated circular spot. Measurements are obtained by use of a high sensitivity, fast rise time photo-diode. For this experiment an E.G.& G., Inc., SGD-100A unit with a rise time of four nanoseconds and a sensitive area of about one millimeter square was used. It is necessary that the sensitive area of the diode be smaller than the width of one circular fringe. Output of the photo-diode was filtered, amplified and displaced along with the acoustic signal on a dual-trace oscilloscope. Fig. 12 shows the block diagram circuit for this sensor system. Fig. 13 shows examples of how rod motion is measured by interpreting output of the photo-diode circuit. With rod motion, each cycle of the diode output corresponds to one-half wavelength of displacement so that for linear motion the amount of displacement between two points in time is equal to the number of cycles of the photo-diode output on the oscilloscope over the same interval of time (See Fig. 13a). If the rod motion is oscillatory then at the peak and trough of the acoustic wave the photo-diode output will reverse direction (See Fig. 13b). This is a result of the rod reaching the maximum point of its travel at a point which is not a multiple of one-half wavelength of light. As the rod motion reverses the light intensity in the fringe pattern must also reverse and thus the inflection in the photo-diode output. This characteristic greatly simplifies the measurement process since one need only count the number of cycles between inflection points of the photo-diode output to determine peak-to peak displacement amplitude of the sampled point. Note in Fig. 13b that

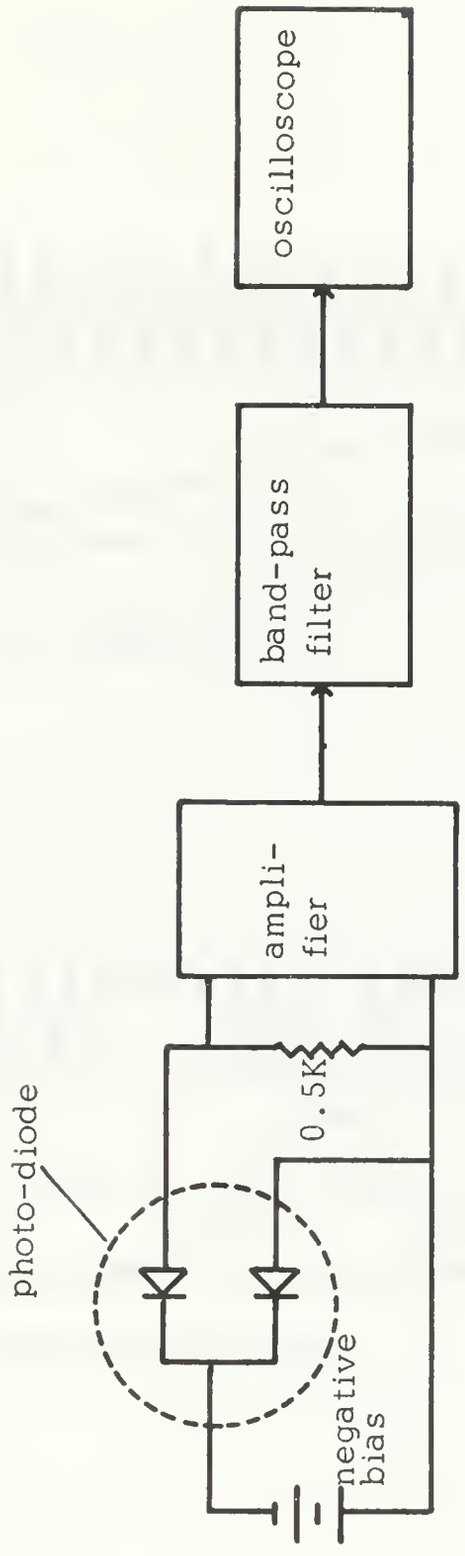

Fig. 12 Photo-diode Circuit

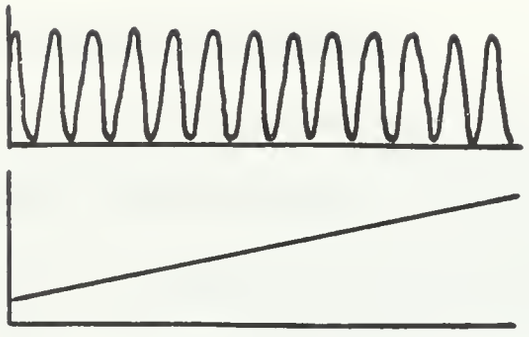

(a) Linear Motion

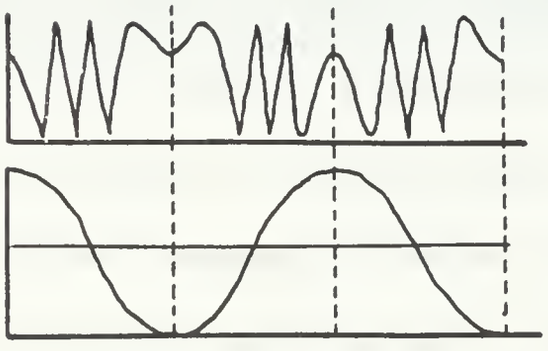

(b) Sinusoidal Motion

Fig. 13 Typical Photo-diode Output

since the rod spends more time near the peak and trough of its sinusoidal motion the frequency of photo-diode output varies over a cycle of motion. Plate III shows an example of displacement data taken with an oscilloscope. Usually, several exposures were made on each print so that redundant data would be available for each sample point at a given frequency thereby enhancing accuracy.

B. Measurement of Directivity Patterns

Directivity patterns for this experiment were measured in the Underwater Sound Laboratory Facility of the University of Texas which is equipped with a pool measuring eighteen feet by twenty-eight feet with a depth of fifteen feet. The experimental system consisted of a signal generation circuit, the cylindrical rod assembly and a pressure sampling circuit.

For this phase of the experiment a pulsed acoustic signal could be used since radiated pressures using pulses were large enough to be measured. The circuit used for signal generation is similar to that described in Chapter II. It is illustrated in Fig. 14. The output of a wide-range oscillator was used as the signal into a tone-burst generator. A second output was connected to a digital frequency meter for accurate frequency indication. The tone-burst generator output was a series of sinusoidal wave-packets. Frequency of the sinusoid was controlled from the oscillator. The number of cycles in each wave packet and the spacing between wave-packets was easily controlled with the tone-burst generator. Typically eight to thirty-two cycles were used in a wave-packet depending upon the frequency. Spacing of about one-half second between pulses allowed reflections to die out. Output of the tone-burst generator was connected to two stages of amplification and then to a matching transformer and finally the

PLATE III

Photo-diode Output for Sinusoidal Input

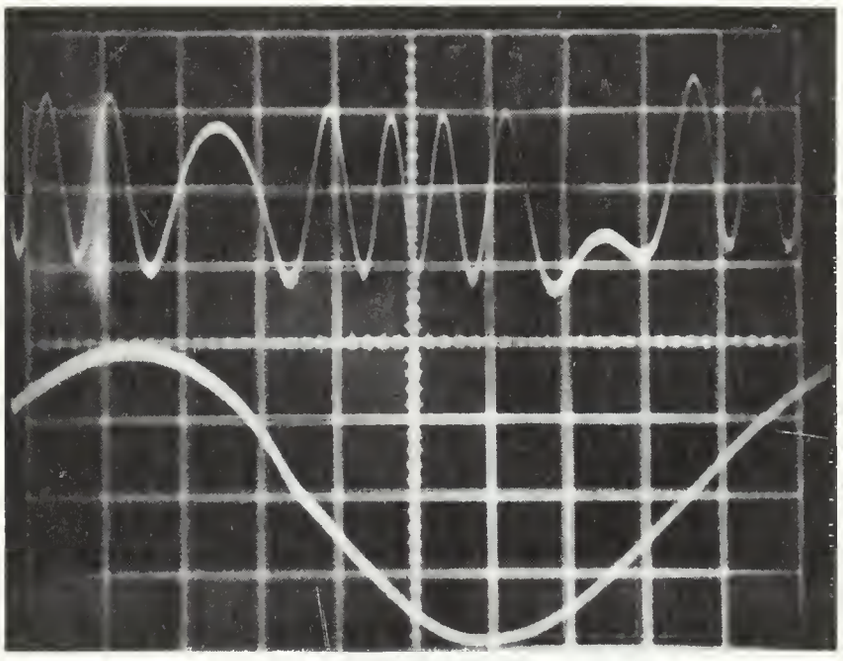

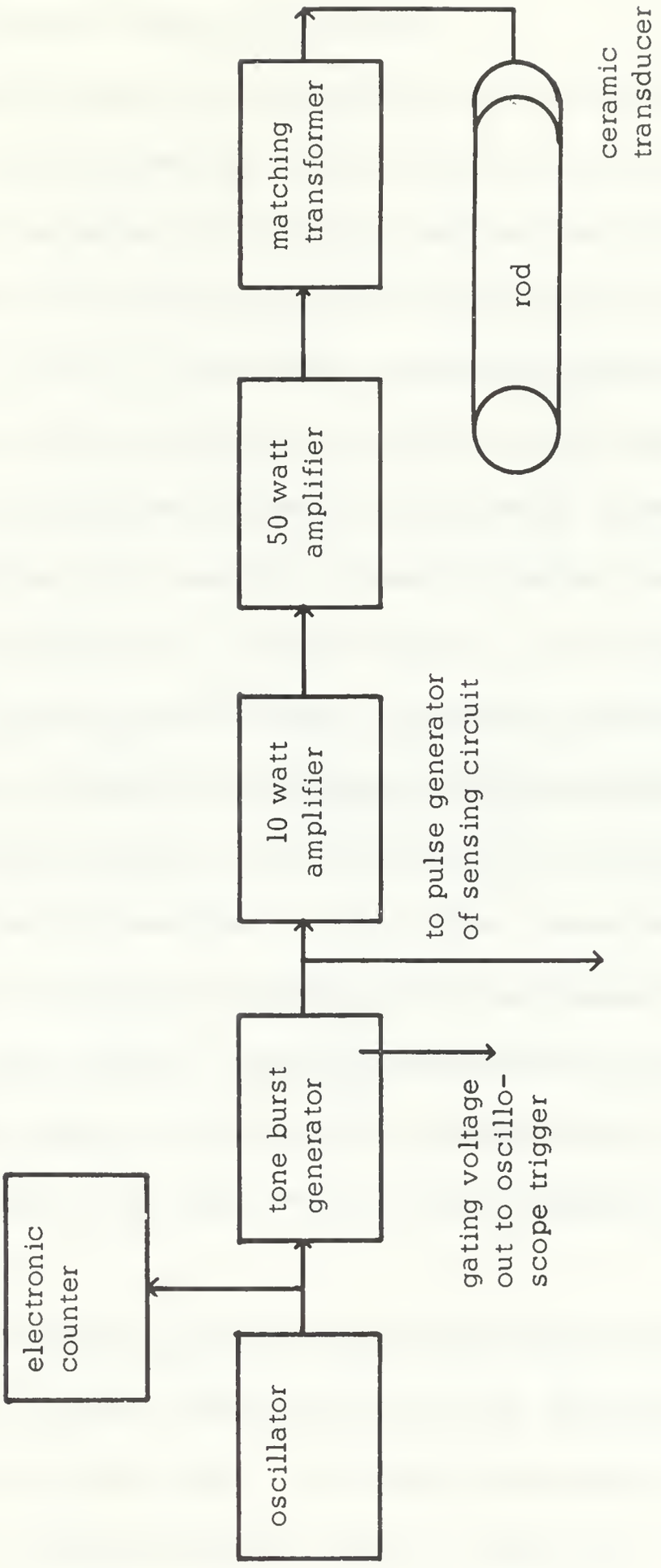

Fig. 14 Acoustic Pulse Generation Circuit

transducer on the cyclindrical rod. Tone-burst output was also transferred to a pulse-generator for use in timing of the system.

The sinusoidal pulses were transmitted to the rod through a water tight hose connection. The rod assembly used was exactly as described in Chapter II. This assembly was suspended from walkways over the laboratory pool so that the axial centerline of the rod was seven feet below the water surface and the radiating face of the rod was at least eight feet from the nearest pool wall.

Fig. 15 is a block diagram of the pressure sensing circuit. Radiated pressure waves in the water were detected by an Atlantic, Model LC-10 hydrophone. The hydrophone was mounted to a radius arm whose pivot point was directly above the radiating face of the rod (See Fig. 16). It was mounted such that the vertical position of the hydrophone and its radial distance could be altered. For these measurements the hydrophone was fixed at the vertical height of the rod axial centerline. Radial distances, from hydrophone to source, of two, four, and six feet were used for taking data. These hydrophone to source distances were well out into the farfield which was calculated to begin at about two inches for a piston radiator. Attaching the hydrophone pivot arm directly to the top of the baffle enabled maintenance of a constant radial distance from hydrophone to source over the range -90° to 90° with respect to the axial centerline of the rod.

From the hydrophone, detected signals were routed to two 40 decibel amplifiers and then through a variable band pass filter (Krohn-Hite, Model 310-C) to enhance the signal to noise ratio. The filtered sinusoidal wave-packet was then connected to a sampling voltmeter (Dranetz, Model 215). The sampling

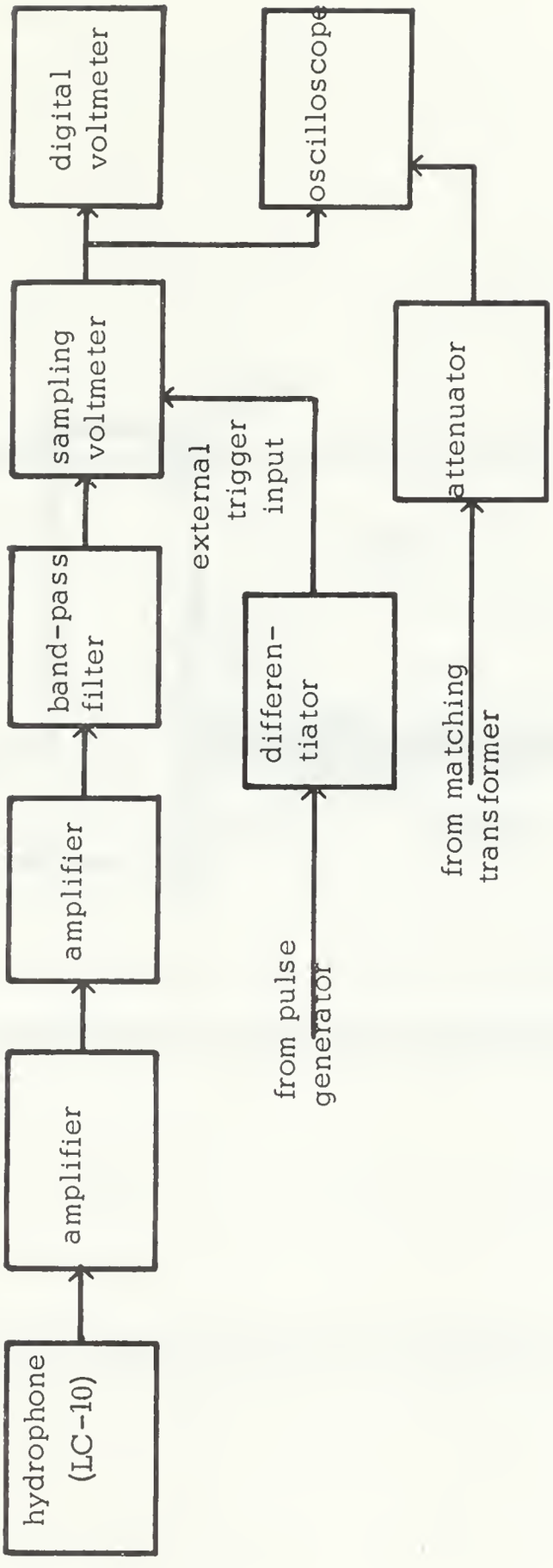

Fig. 15 Acoustic Pressure Sensing Circuit

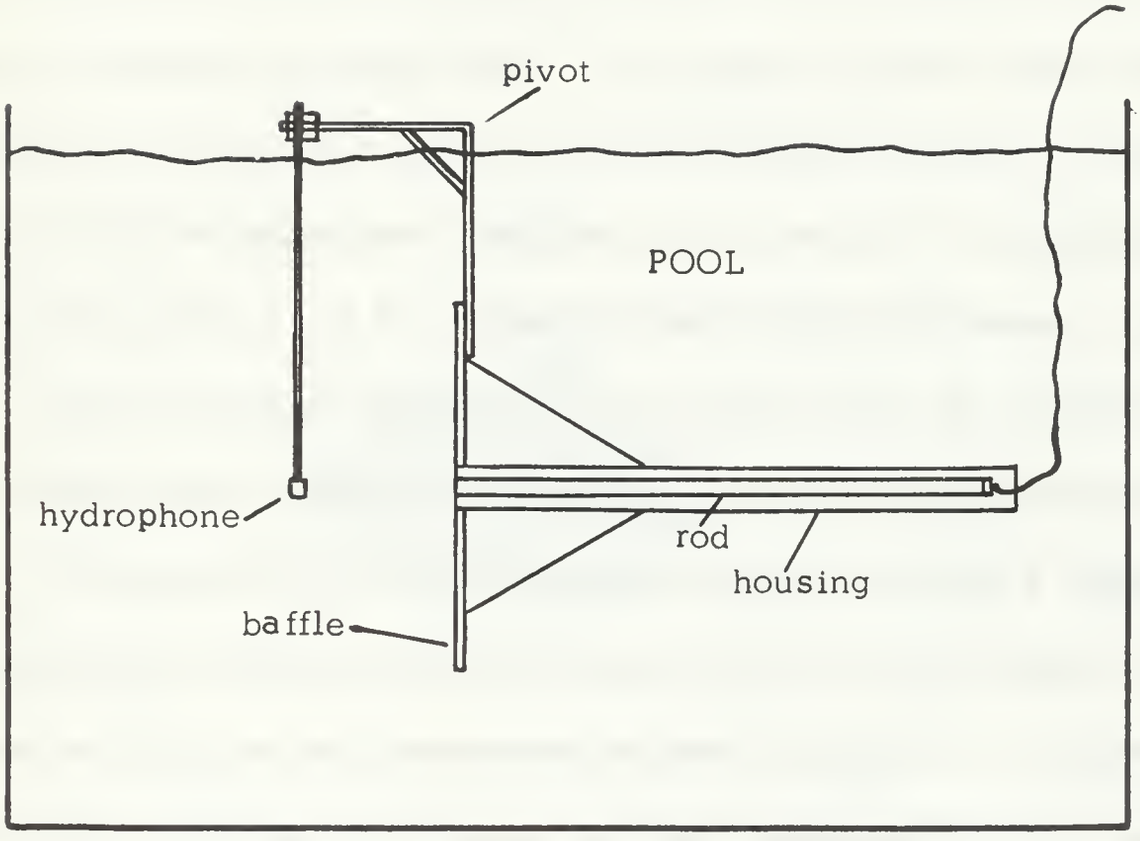

Fig. 16 Cylindrical Rod Assembly in Pool (side view)

voltmeter was externally triggered by a variable delay output from a pulse-generator (General Radio Corp., Model 1217-C). The trigger voltage had the form of a negative spike after differentiating the square wave output of the pulse-generator. The pusle-generator was triggered by the output of the signal generating tone-burst generator. Thus by adjusting the pulse duration control on the pulse-generator, timing of the negative spike trigger to the sampling voltmeter could be controlled to initiate sampling only during the steady-state portion of the detected pressure signal. The length of sample taken of the signal voltage waveform was controlled at the sampling voltmeter. Outputs from the sampling voltmeter were presented on one trace of an oscilloscope (Tektronix, Type 535-A) and on a digital voltmeter (Hewlett-Packard, Type 3430-A). The oscilloscope presentation was used to show the received acoustic pressure signal and to indicate which portion of the incoming signal was being sampled. An internal circuit of the sampling voltmeter provided a "pedestal" on the oscilloscope directly over the portion of signal being sampled. Fig. 17 shows how the oscilloscope presentation typically appeared. The digital voltmeter was used to provide an accurate amplitude measurement of the sampled portion of the signal wave-packet.

Angular position of the sensing hydrophone was determined by rigidly mounting a large protractor to the framework directly below the pivoting arm. To measure the directivity patterns the desired frequency, pulse length and pulse repetition rate were set, the sampling voltmeter was set to trigger during the steady-state portion of the pulse, and then voltage readings were taken as a function of hydrophone angular position. Conversion of the voltages to

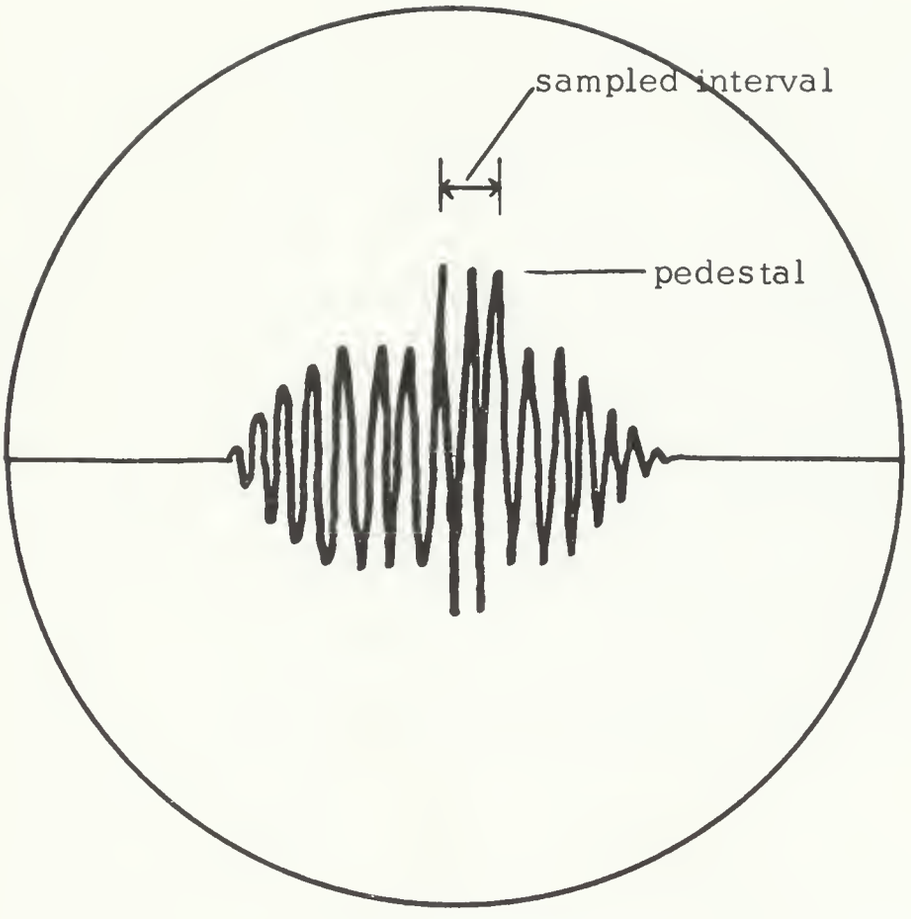

Fig. 17 Representation of Oscilloscope Picture of Sampled Waveform

decibels relative to the axial voltage reading and then plotting the results on polar graph paper yielded the desired radiation patterns.

CHAPTER IV

THE EXPERIMENTAL RESULTS

A. Displacement Profiles and Discussion

Figures 18 - 24 represent the results of the displacement profile measurements. The abcissa of each graph is expressed as a normalized radial co-ordinate (r/a), where r is the radial position and "a" is the actual radius of the rod. The radial positions then go from zero at the axial centerline to one at the cylindrical surface of the rod. The ordinate of each graph represents peak-to-peak normalized axial particle displacement and is expressed as (w_r/w_o) where w_r is the particle displacement at radius r and w_o is the axial displacement for r equal to zero. Accuracy of the displacement profile measurements is limited by one's ability to resolve a fractional portion of one cycle of the photo-diode output. If one assumes that one-sixteenth of a cycle can be resolved and recalls that as frequency increased from 10 to 85.8 KHz photo-diode output went from six cycles to one-half cycle between inflections, the expected error can be shown to vary from less than 2.0% at 10 KHz to about 25% at the highest frequency.

In Fig. 18 one can see that at the lower frequencies the deformation of the rod face is dome shaped. The total displacement profile could be thought of as being made up of a component of uniform axial displacement plus a component of deformation. In that light the deformation goes from zero at the outer edge of the rod to a maximum on the axial centerline. Although the curves do not show absolute values of displacement it is of interest to note that the

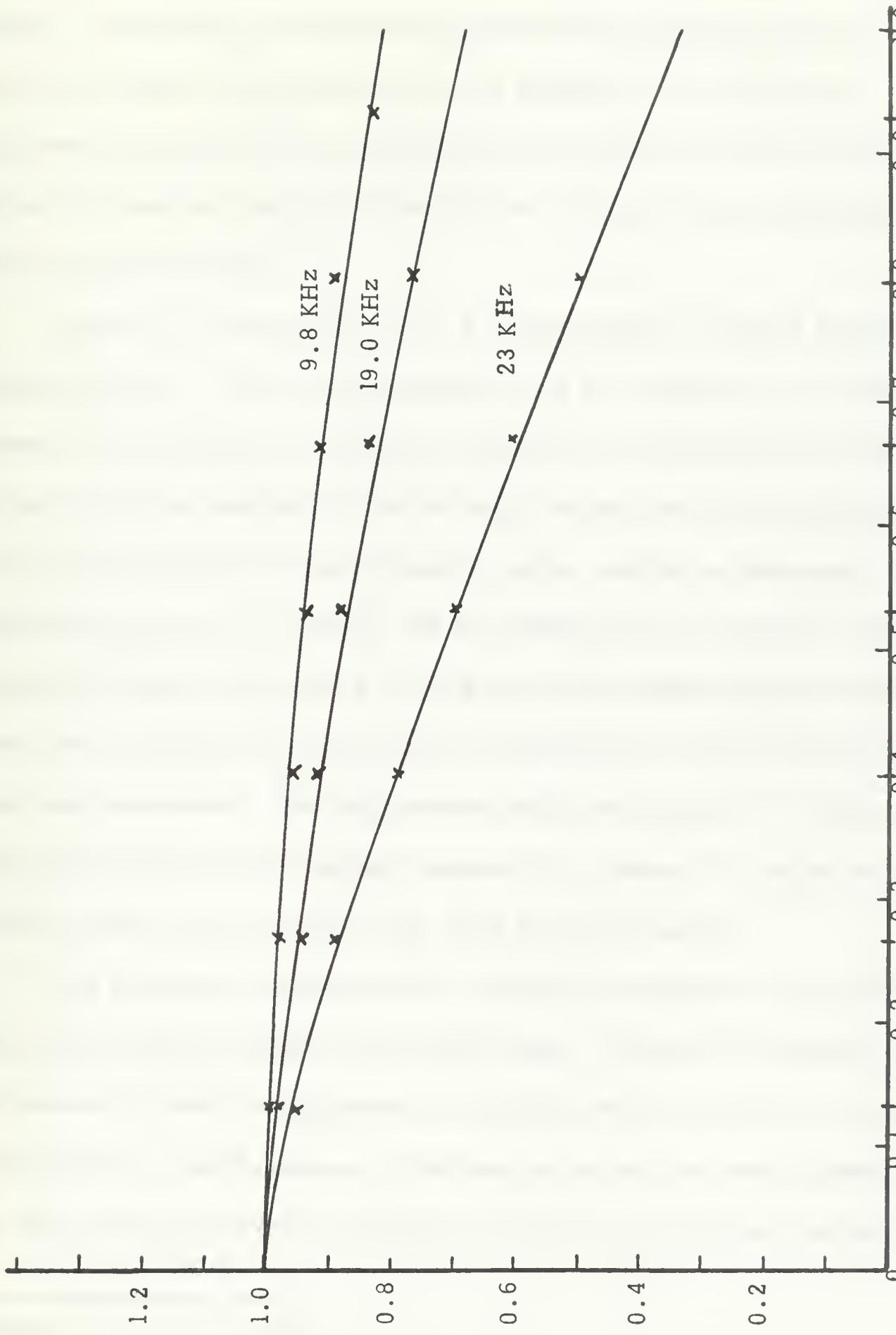

Fig. 18 Axial Displacement Profiles for 9.8, 19.0, and 23 KHz

largest absolute displacement achieved in this experiment was about 2.0 microns. As frequency increased the displacement went down. Here-in was one of the greatest difficulties involved in conducting this experiment. This displacement limitation actually precluded measurements beyond 86 KHz. Note that at the lower frequencies the deformation of the rod face increased as frequency was increased.

At about 29 KHz (See Fig. 19), a minimum began to appear in the displacement profiles. This is often referred to in the literature as a "nodal cylinder" of displacement in the rod, although the displacement was not zero. The nodal cylinder remained in the rod for all subsequent measurements above 29 KHz although it did not remain fixed in radial position or magnitude. By comparing Figures 19, 20, and 21 one can observe that as frequency was increased between 29 KHz and 47.5 KHz the nodal cylinder progressed steadily toward the centerline of the rod while the characteristic dip in the profile became more pronounced. The displacement profile measured at 47.6 KHz most closely approximated the condition referred to by Maxwell* in which he predicted an actual zero of motion at the node for one frequency.

At a frequency of approximately 50 KHz the magnitude of axial displacement at the minimum became significantly higher. Figures 22 through 24 show this increase in nodal displacement as compared with that of Fig. 21. This corresponds to a smaller amount of deformation around the nodal cylinder. Note also that for these upper three frequency samples the reduction of deformation

---

*Maxwell, op. cit., p. 33.

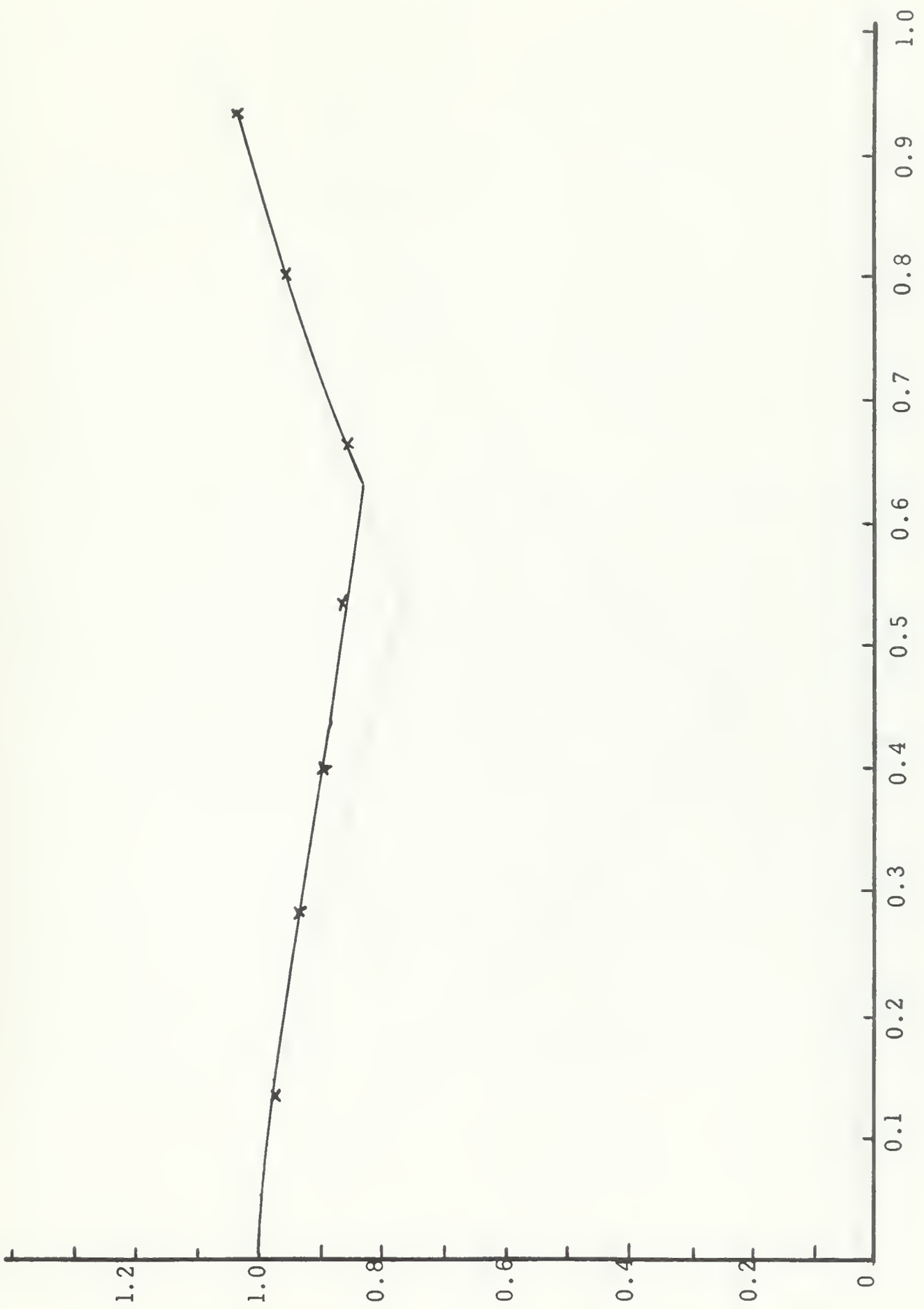

Fig. 19 Axial Displacement Profile for 29.1 KHz.

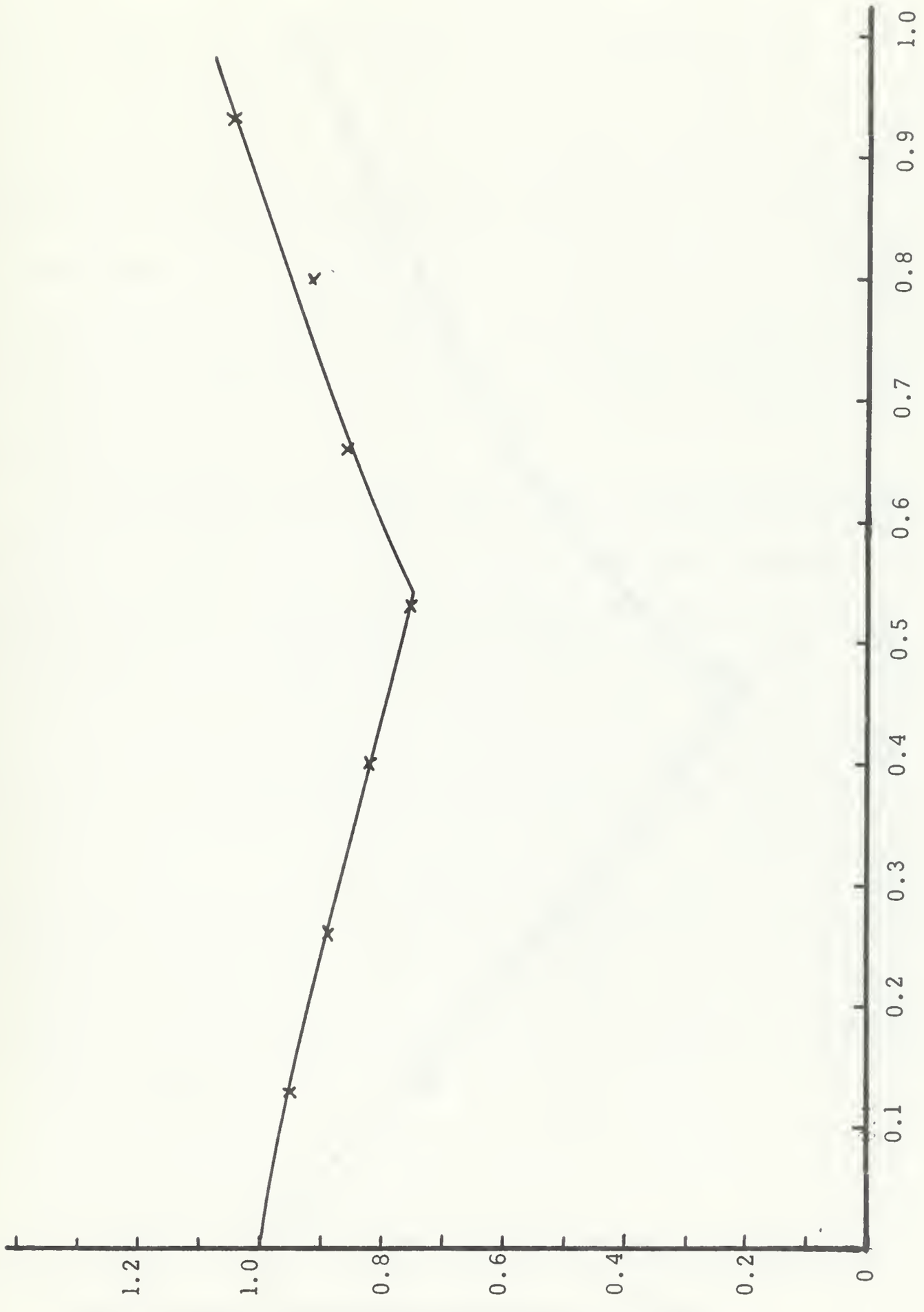

Fig. 20 Axial Displacement Profile for 33.4 KHz

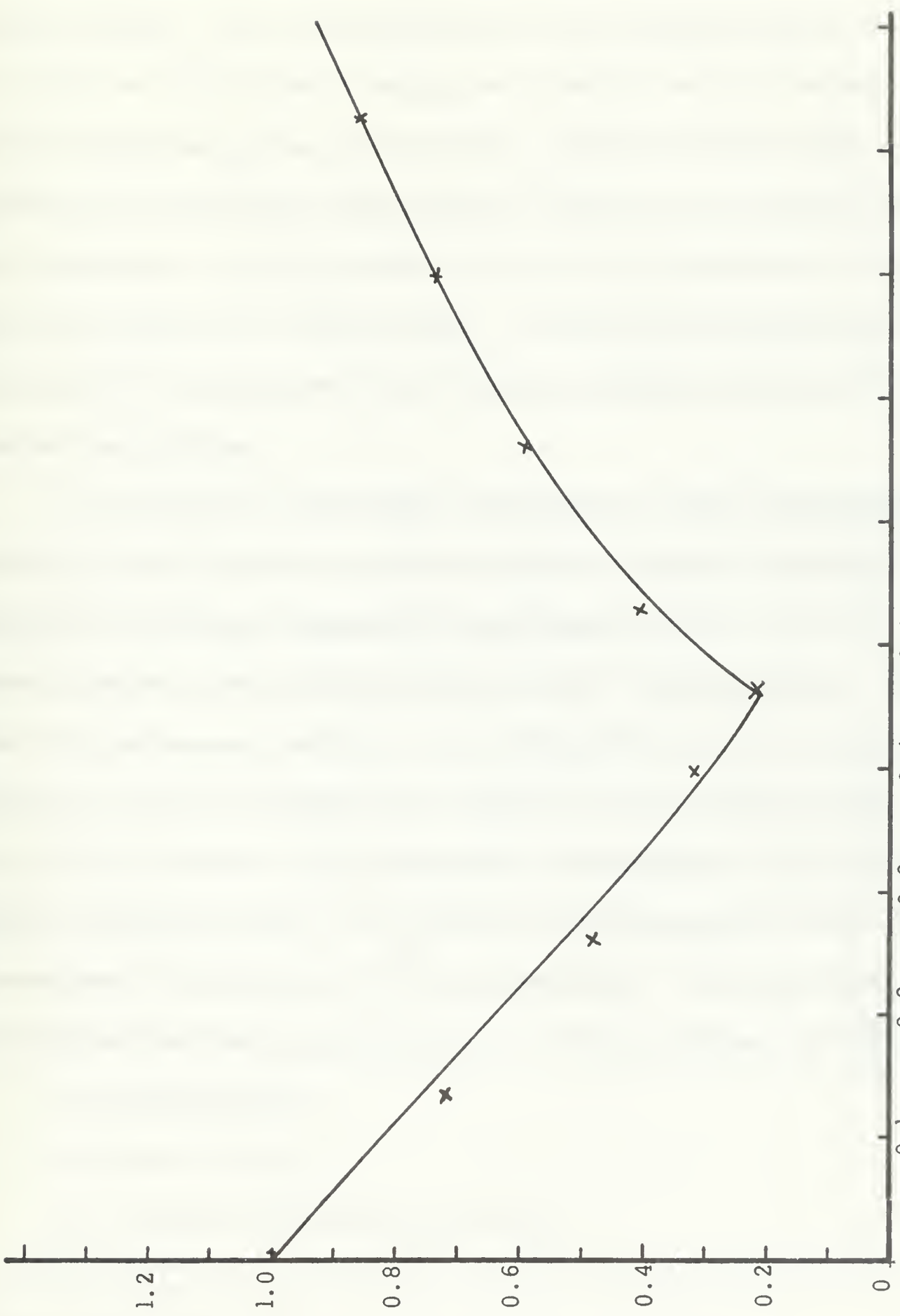

Fig. 21 Axial Displacement Profile for 47.6 KHz

at the nodal cylinder is balanced by a much larger displacement at the outer surface of the rod. The axial displacement at the cylindrical surface of the rod, which can be attributed to propagation of surface waves, is actually greater than the displacement at the rod centerline. Note also that once again as frequency was increased the nodal cylinders tended to move inward and become more pronounced. The only exception to this is that the magnitude of displacement at the node for 85.8 KHz increased. It is felt that the limited accuracy of the displacement measurement at this frequency probably accounts for the indicated inconsistency.

In comparing the experimental measurements of axial displacement profile with those calculated from existing theory it becomes immediately evident that a significant discrepancy exists between the two. Fig. 25 indicates the calculated radial distribution of axial velocity profiles.* They differ from displacement profiles by only a multiplicative term, $j\omega$, thus comparison of these normalized values with the measured values is valid. In Fig. 25 the ordinate is a non-dimensional value identical to that used for plotting experimental results. The abcissa is non-dimensional velocity which is normalized to the value one at the axial centerline. Each curve shown is for a different non-dimensional frequency, Ω, which is defined, $\Omega = \frac{\omega a}{C_s}$ where,

ω = radian frequency

a = radius of the rod

C_s = velocity of shear waves in the rod.

---

*Maxwell, op. cit., p. 33.

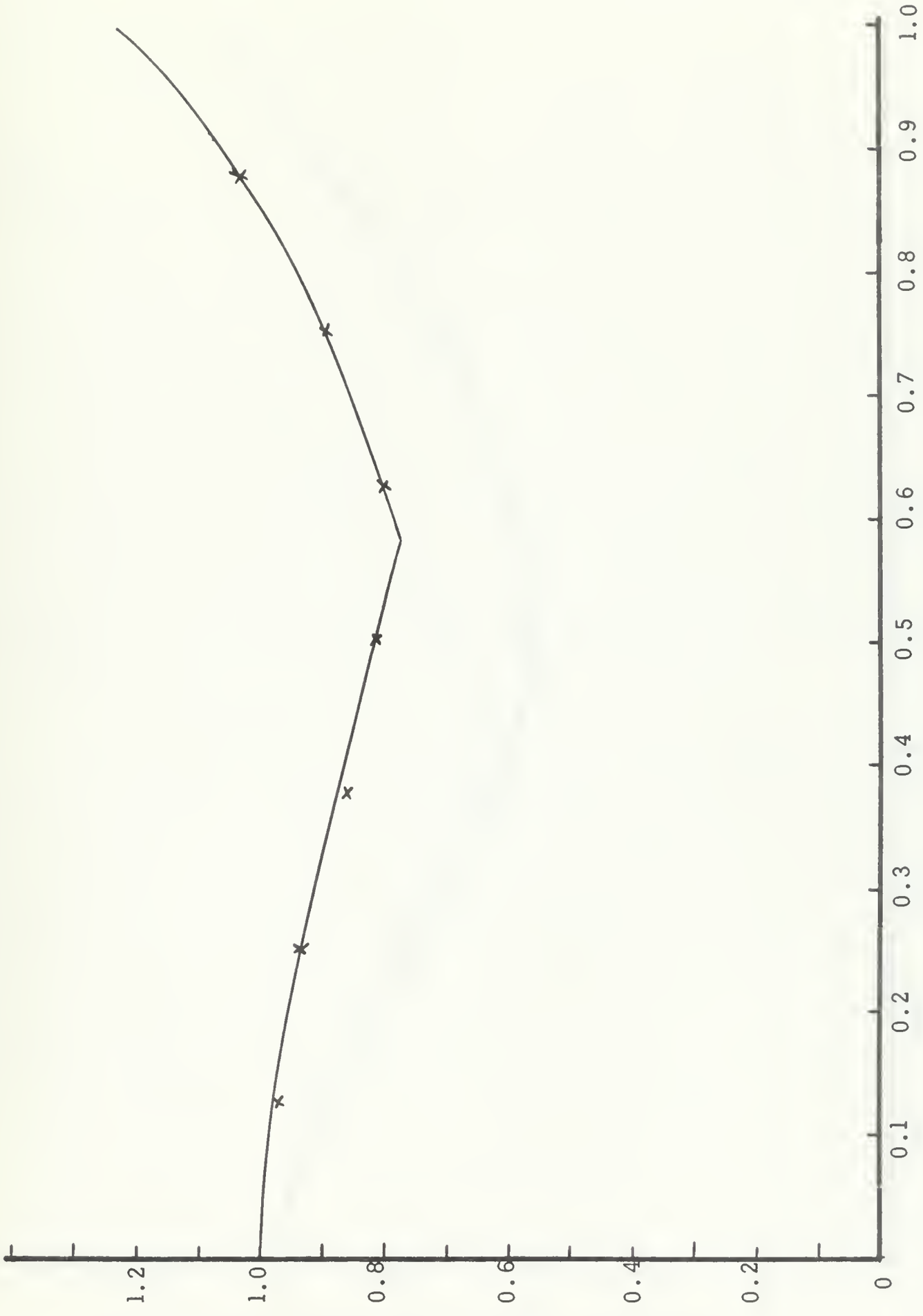

Fig. 22 Axial Displacement Profile for 61.5 KHz

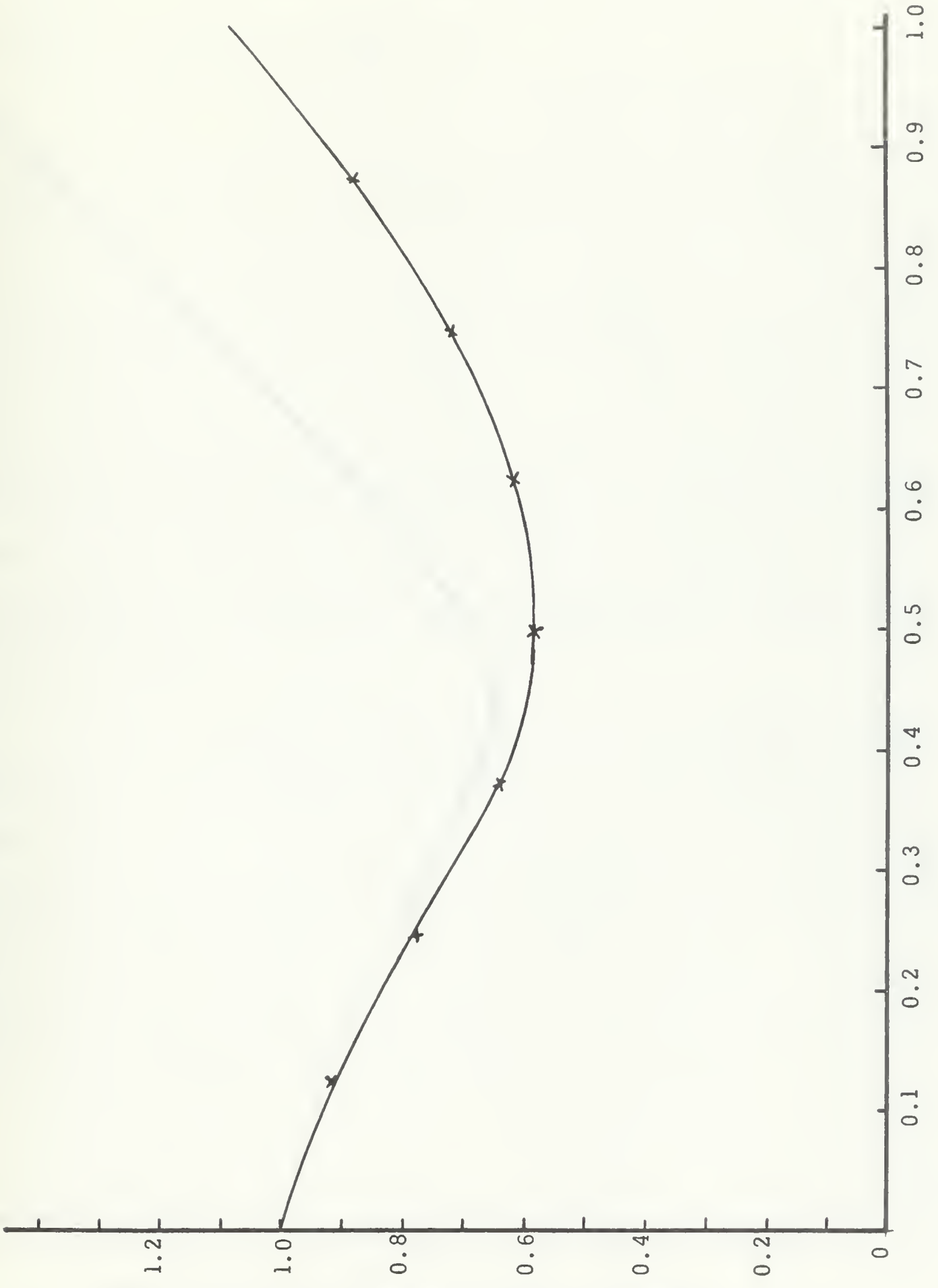

Fig. 23 Axial Displacement Profile for 68.5 KHz

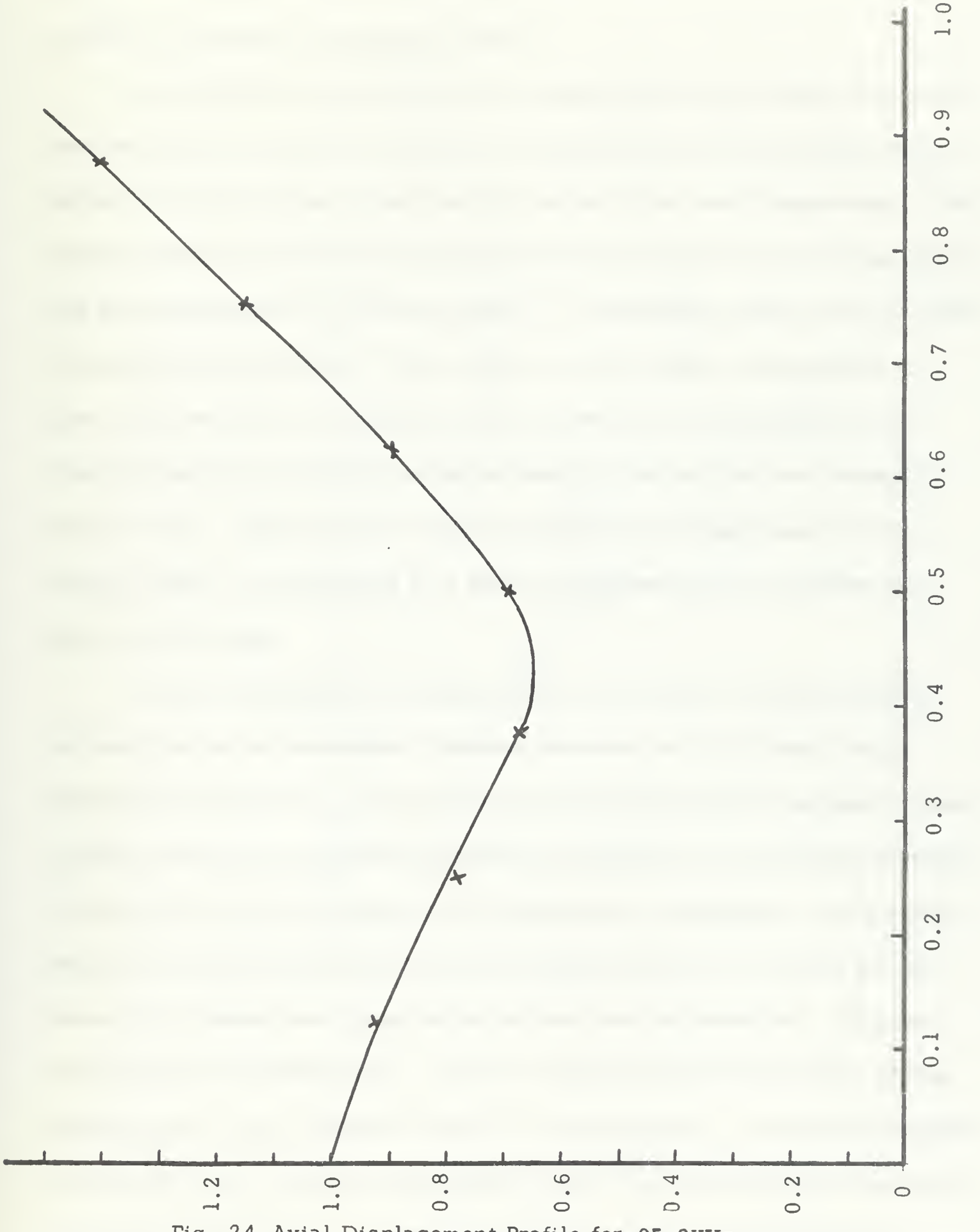

Fig. 24 Axial Displacement Profile for 85.9KHz

In relation to the rod used for this experiment the value can be simplified to, $\Omega = f/25$, where f is frequency in KHz.

In comparing the measured displacement profiles with those calculated note that up to 23.1 KHz the profiles are similar although the measured curves indicate a greater degree of deformation even at these lower frequencies. This tendency toward greater deformation than predicted would lead one to anticipate that the development of a "nodal cylinder" of displacement might occur at lower frequencies than predicted. This, in fact, was the case as comparison of Figs. 18-24 with Fig. 25 indicates. The on-set of a "nodal cylinder" was observed beginning at 29 KHz while the predicted occurrence lies between 50 and 62.5 KHz. The frequency at which the minimum of displacement in the "nodal cylinder" occurred was 47.5 KHz as compared with a calculated frequency of 87.5 KHz.

A brief investigation was conducted in an attempt to reveal possible explanations for the discrepancy between measured and calculated results. Noting that phenomena, such as on-set of the "nodal cylinder" seemed to occur at about one-half the predicted frequency of occurrence, the possible presence of the second harmonic frequency in the signal was considered. Using photographs of the photo-diode output from the interferometer, as in Plate III, the shape of the stress wave signal at the rod end was reconstructed. This was accomplished by plotting time, t, on the ordinate and the total number of axis crossings from a zero reference time to t on the abcissa. The distance between two adjacent axis crossings of the photo-diode output corresponds to motion of the sampled point equal to one-half wavelength of the laser light used to

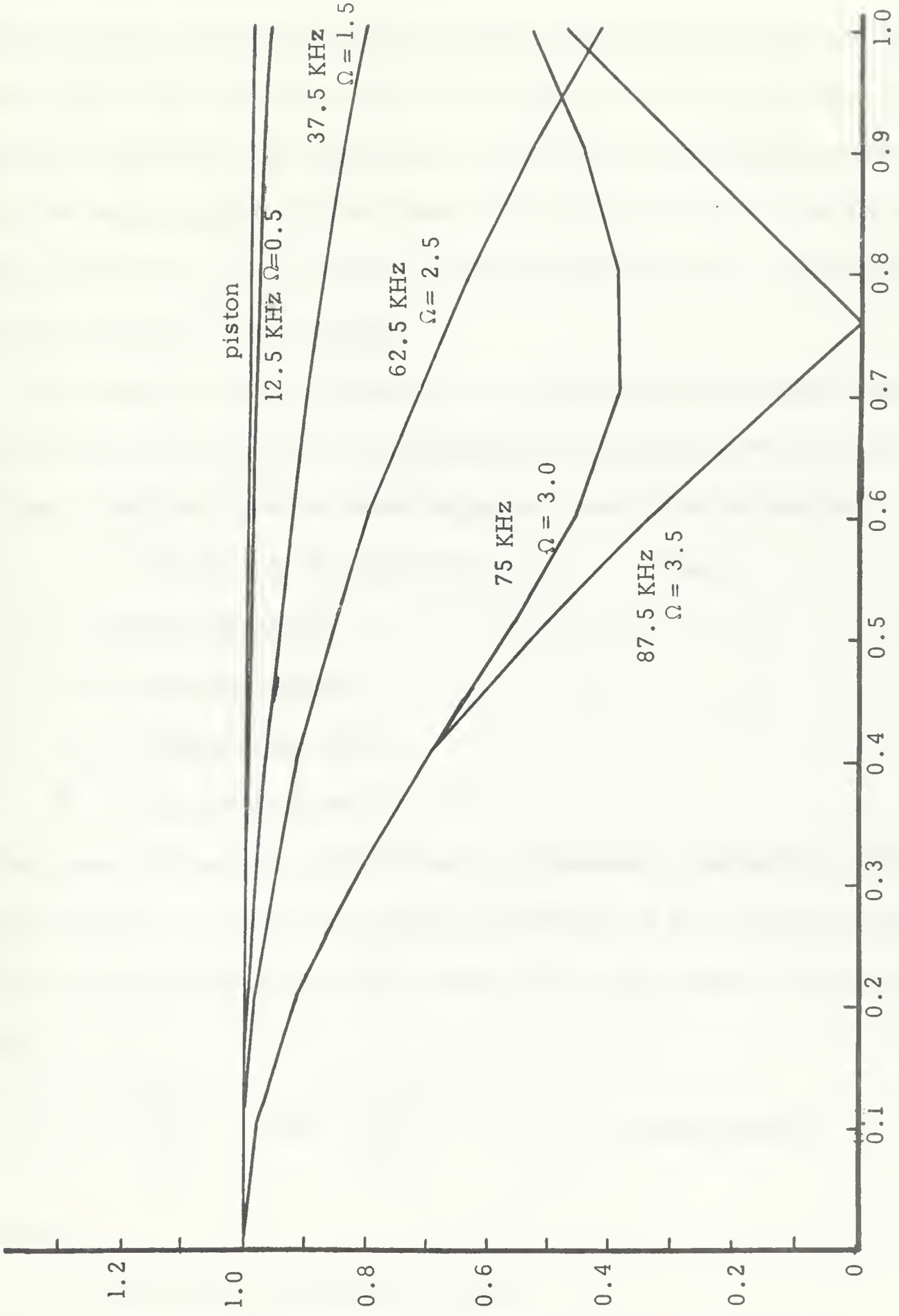

Fig. 25 Axial Displacement Profiles Predicted by Mathematical Model

illuminate the point. If the reconstructed motion of the sampled point was a distorted sinusoid, then the presence of higher order harmonics would be implied. One then might expect results similar to those expected for some multiple of the fundamental frequency of the stress wave. Fig. 26 is an axial displacement versus time reconstruction for three radial points at 10.52 KHz. It clearly shows that the stress wave signal was not significantly distorted, thus second harmonic signal was deemed to be not present.

The investigation then shifted to a consideration of the existing theory. For the sake of completeness a brief background on Maxwell's* work is provided here. Beginning with the vector equation of motion for an ideal rod,

$$(L+2G)\,\nabla\,(\nabla\cdot\bar{D}) - G\nabla x\,\nabla x\bar{D} = \rho_s\,\ddot{\bar{D}} \qquad \text{where,}$$

L, G = Lame' constants

$\bar{D}$ = vector displacement

ρ_s = density of the solid

$\ddot{\bar{D}}$ = second time derivative of $\bar{D}$,

solutions were obtained for radial and axial displacements and radial, axial, and shear stresses. Applying the boundary conditions of the vanishing of radial and shear stresses on the cylindrical surface of the rod resulted in Pockhammer's equation,

$$\frac{(b^2 - s^2)^2}{2p}\,\frac{J_o(p)}{J_1(p)} + 2sb^2\,\frac{J_o(s)}{J_1(s)} = \Omega^2 \qquad \text{in dimensionless}$$

form where,

b = complex axial propagation constant

---

* Maxwell, op. cit., pp. 7-30.

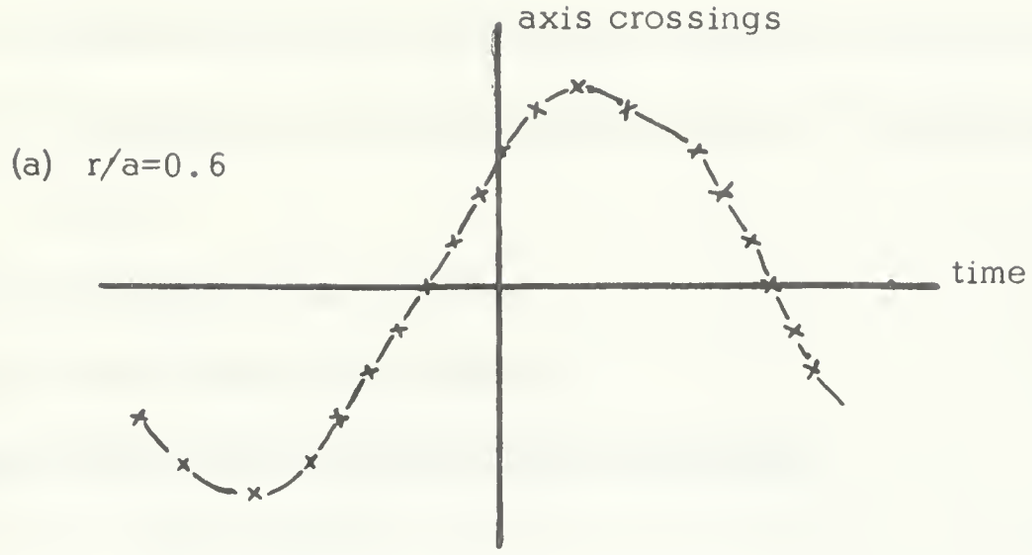

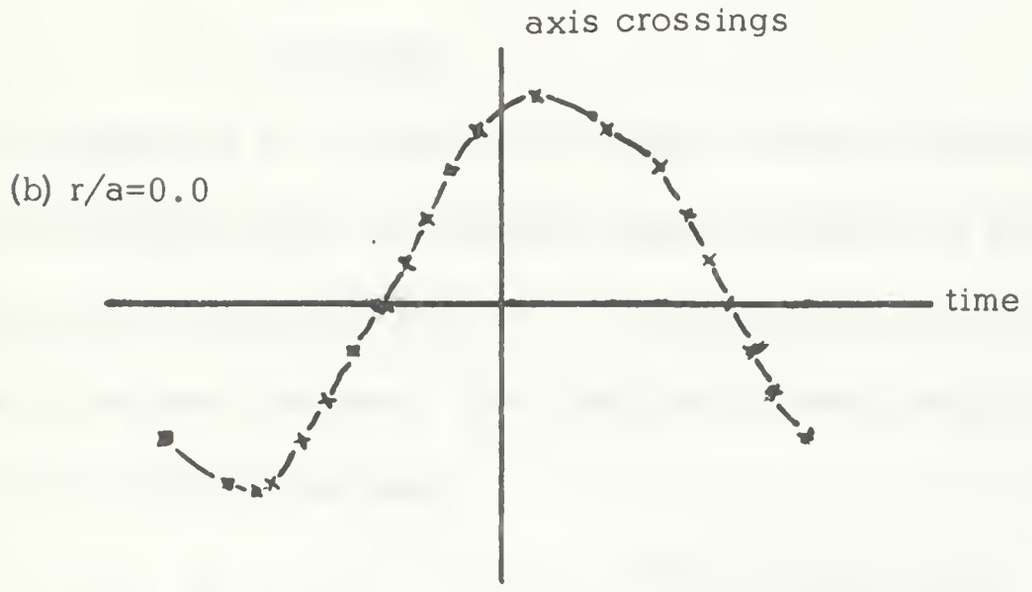

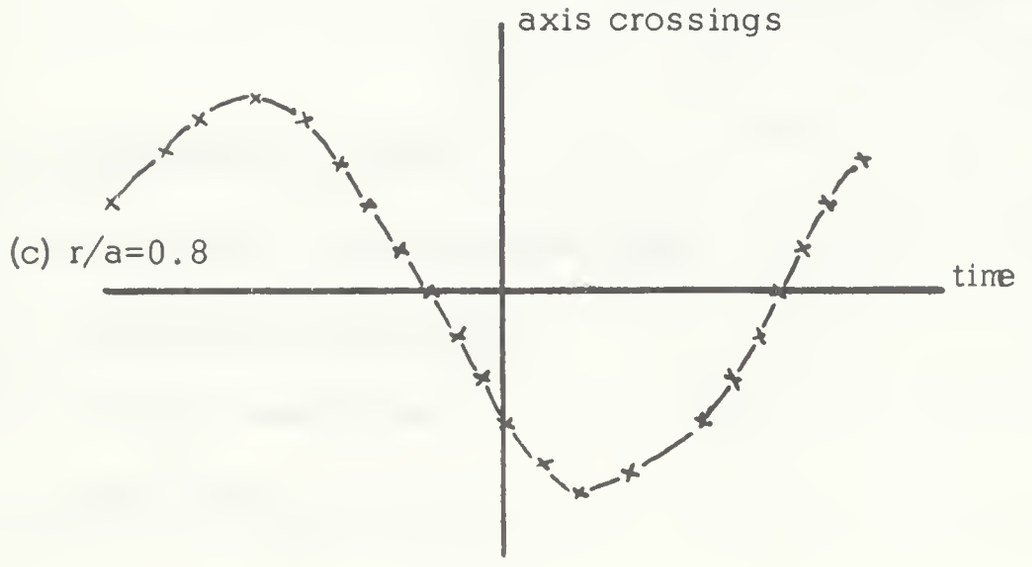

Fig. 26 Axial Displacement versus Time for Various Radial Points

s = dimensionless radial propagation constant for shear waves

p = dimensionless radial propagation constant for compressional waves

J_o = zero-oder Bessel function

J_1 = first-order Bessel function

Combining Pockhammer's equation with the identities,

$$\Omega^2 = s^2 + b^2$$

$$\delta^2\Omega^2 = p^2 + b^2$$

$$\delta^2 = G/(L+2G)$$

allowed calculation of p, b, and s if the values of Ω and δ were known. Assuming an infinite number of solutions, called branches, to Pockhammer's equation exist led to the expression of the velocities and stresses as infinite sums over the allowed branches. The final form for axial velocity used by Maxwell in his calculations was,

$$V(\sigma, \zeta = 0) = \frac{A}{a^2} \sum_{n=1}^{\infty} b_n J_o(p_n\sigma) \left[1 + \frac{2P_nS_nJ_1(p_n)\,J_o(s_n\sigma)}{(b_n^2 - S_n^2)\,J_1(s_n)\,J_o(p_n\sigma)}\right](\delta_{1n} + R_n)$$

where,

V = dimensionless velocity

σ = dimensionless radial position (r/a)

δ_{1n} = Kroenecker Delta function

R = reflection coefficient

$(\ )_n$ the n^{th} branch of $(\ )$.

A digital program, "FIELDS"*, was written to compute velocity and other field quantities for various rod materials and frequencies. (A copy of this program was kindly supplied by G. G. Maxwell to the author and was used as the basis for this investigation).

Looking at the above velocity equation one sees a "perturbation-like" expression inside the summation, in the factored form $x(1 + \epsilon)$. The second term in brackets corresponds to epsilon in the expression. It should be a second-order correction term. For b_n equal to S_n the entire equation is undefined and should not be used. For b_n not close to S_n the second term inside the brackets should be small compared with one. Therefore, one should be justified in approximating for the velocity profile,

$$V(\sigma, \zeta = 0) = \frac{A}{a^2} \sum_{n=1}^{\infty} b_n J_o(P_n \sigma) (\delta_{1n} + R_n)$$

Using the digital program "FIELDS" an analysis of the equation for velocity profiles showed that the second term in brackets had a large effect on the velocity profile. This term, in fact, was responsible for "washing-out" an expected radially inward progression of the "nodal cylinder" of motion with increasing frequency, needed to duplicate experimental findings. To demonstrate this, Fig. 27 shows the solution for the isolated second branch contribution to velocity profile over the frequency range 12.5 to 62.5 KHz. Note that the "nodal cylinder" remained at a fixed radial position for all

---

*"FIELDS", Digital Program, Appendix I.

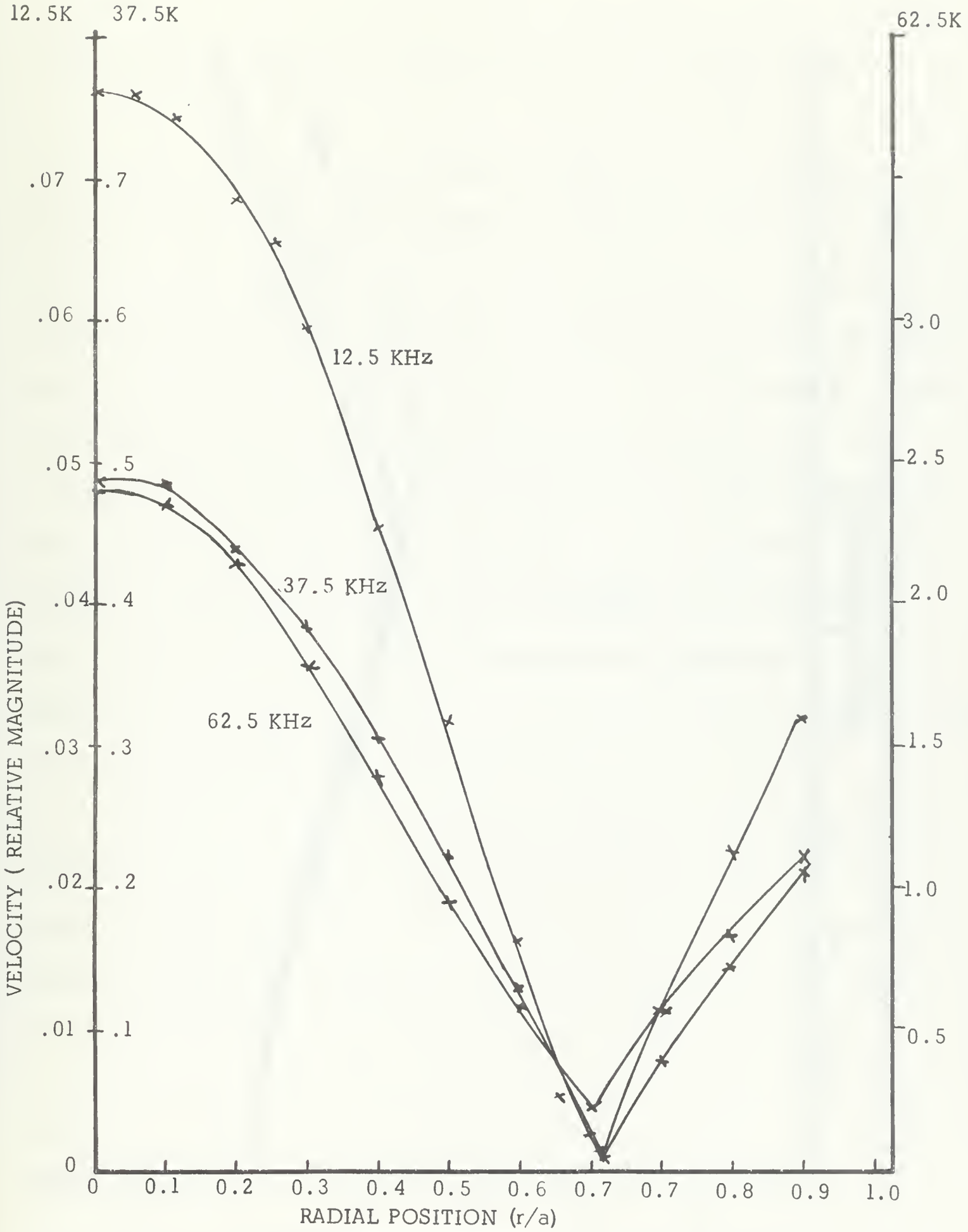

Fig. 27 Second Branch Contribution to Velocity Profile for Various Frequencies

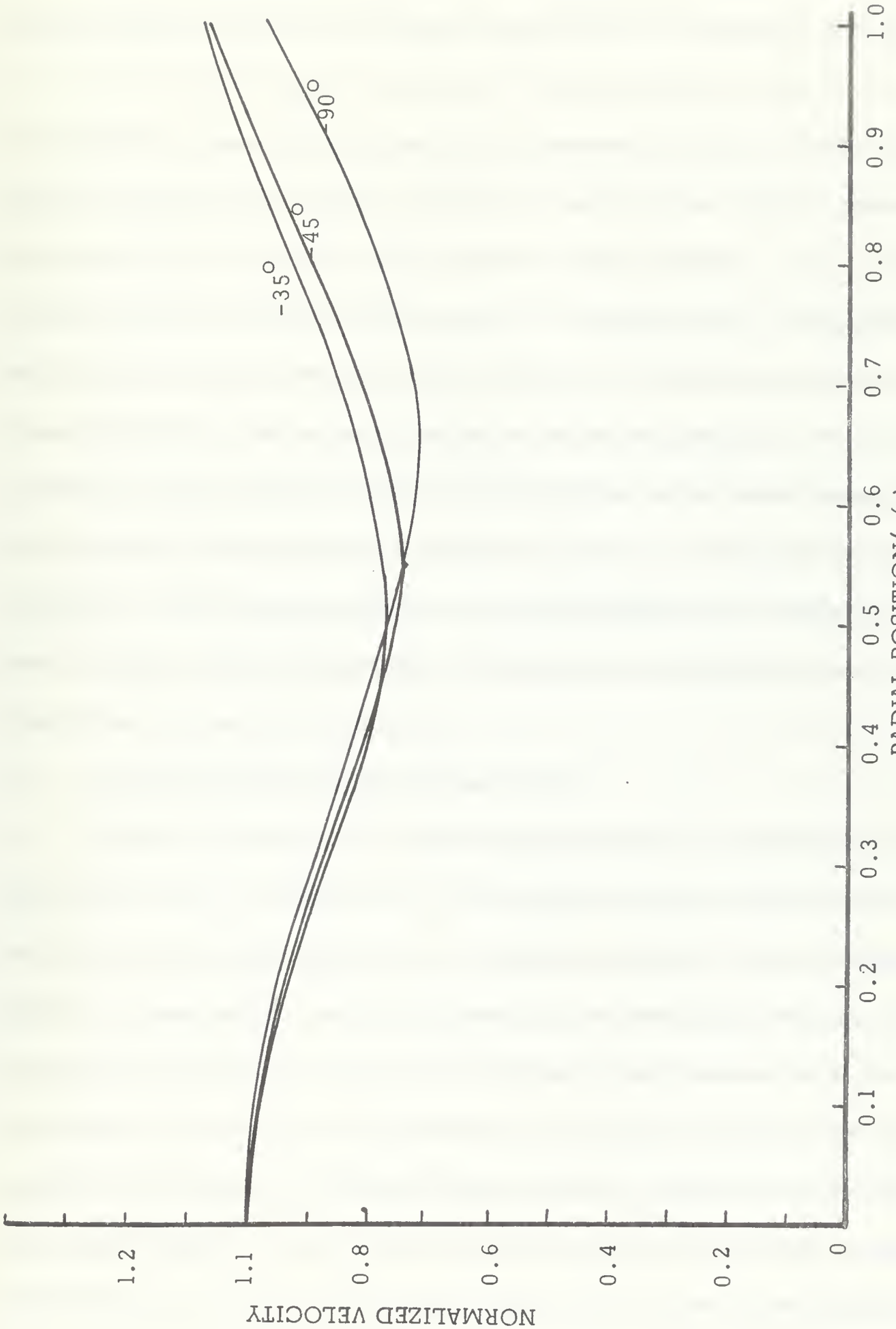

Fig. 28 Summation of Velocity Branches One and Two for Various Phase Relationships

frequencies. The results of velocity profile computations with the second term in the brackets omitted more closely approximated the measured profiles.

In a further attempt to determine whether elements of the theory could be combined to more closely approximate measured results a "Fourier series type" construction was tried. Calculated results of the "FIELDS" program for only the first two branches of the summation were combined. Fig. 28 shows the result of summing branches one and two at a frequency of 37.5 KHz with a phase shift, constant across the rod face, applied to the branch two solution. In this case, the shape of the velocity profile including the position of the "nodal cylinder" is quite similar to the measured profiles in the same frequency range. Although this analysis showed that elements from the existing theory can be combined to approximate closely the measured displacement profiles a more detailed study of the significance and correctness of separate terms in the theoretical expressions is called for.

B. Pressure Distributions and Discussion

Results of directivity pattern measurements for the radiating rod are illustrated in Fig. 29 through 34. Error in these pressure measurements resulted from inaccuracies inherent in both the sampling voltmeter and the digital voltmeter which reads the output from the sampling voltmeter. These electronic measurement errors are insignificant when compared with the variations in data which occur because of the physical system itself. For example, the sampling voltmeter-digital voltmeter combination may read the data point voltage to within 0.01 volt while the data point voltage is itself fluctuating over 0.2 volt. The major source of error then is attributable to the

process of taking a visual average of digital voltmeter indications at each data point. At any rate, the data can be considered to be accurate to within one decibel.

The pressure distributions for the lower frequencies (Fig. 29) were quite similar to theoretical predictions for plane piston motion at low frequencies. The difference that exists is that the patterns are somewhat wider than for piston motion except that Fig. 29 shows a drop, at 10 KHz, of about eight decibels from the centerline to 90°. For ideal piston motion at the same frequency the expected drop in pressure would be only about two decibels.

As frequency was increased the beam width decreased as expected, but the main lobe was wider because to the dome shaped surface the effective diameter was less. Only a single lobe existed up to about 30 KHz at which point the first side lobe began to develop. Notice on Fig. 31 the existence of a null at 89° from centerline. This occurrence of the null in pressure distribution corresponds with the first occurrence of the "nodal cylinder" in axial displacement profiles. Because of the "nodal cylinder" effect the main beam is flatter and borader than for a piston. At the frequency 47.5 KHz a second side lobe began to appear. Note in Fig. 32 that minima occur at 67° and 85° from centerline. At a frequency 61.5 KHz the minima had rotated toward the axial centerline (See Fig. 33) and now occurred at 55° and 75° with a maximum decrease in pressure level of 26 decibels at the first minimum. Finally, for the highest frequency measured, a third side lobe appeared as in Fig. 34. The first node was rotated to 40° from centerline with the second and third nodes occurring at 60° and 83°. The maximum decrease in pressure level was 20 decibels at the

third node.

Figs. 35 and 36* show theoretical predictions for the radiation patterns of an aluminum rod in water. Results are indicated for both the plane piston approximation (identical to those superimposed on measured radiation patterns) and the rod problem as modeled by Maxwell over the frequency range 12.5-87.5 KHz. Comparison of Figs. 29 and 30 with Fig. 35 points out the similarity of predicted data to the measured values for low frequencies. Note again that the radiation pattern for plane piston motion matches the measurements quite well. This is expected since the radiating rod end is only slightly distorted at these lower frequencies. As mentioned before it can be seen that the only difference between the modeled and measured curves is that at the sides the models do not decrease in level as rapidly with angle as do the experimental data. At the mid-range frequencies considerable differences appear between predicted and measured radiation patterns. At frequencies 30-47.5 KHz recall that the measured displacement profiles already had "nodal cylinders" while the mathematical model did not. Thus a large discrepancy in radiation patterns would be expected. In fact, the predicted radiation patterns for double these frequencies, where nodal cylinders also occurred in the model, would appear to compare more closely with the experimental data.

At the highest frequencies there is also little agreement between predicted and measured radiation patterns. It should be noted, however; that with increasing frequency the measured patterns continue to follow the trend

---

*Maxwell, Op Cit, pp 36, 37.

toward more lobes and progression of the axially symmetric lobes toward the zero axis. The theoretical radiation patterns do not follow this trend (although predicted plane piston patterns do), but instead the model's rod null disappears somewhere between 62.5 and 75 KHz. Then as frequency increases above 75 KHz a single null again begins to move in from the side of the pattern toward the zero axis.

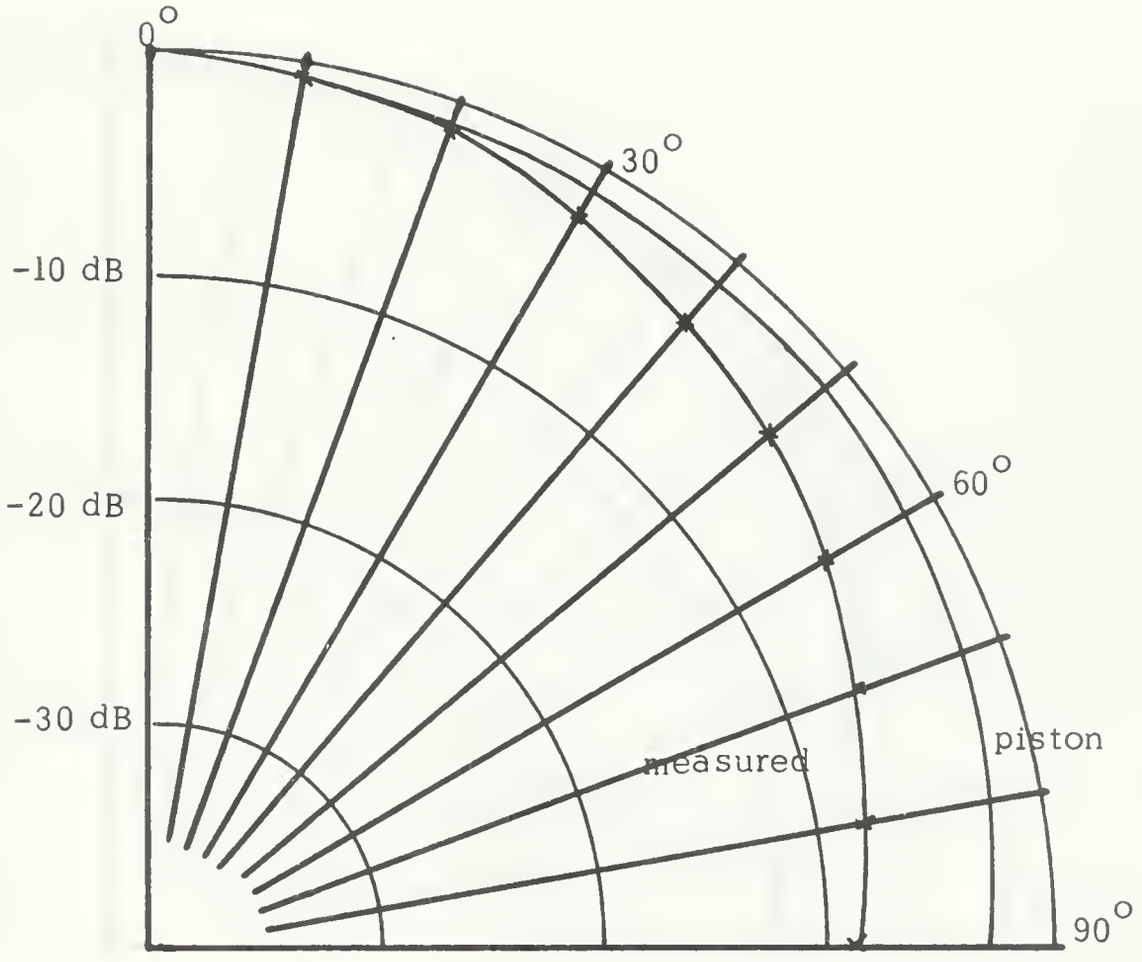

Fig. 29 Pressure Distribution for 10.5 KHz

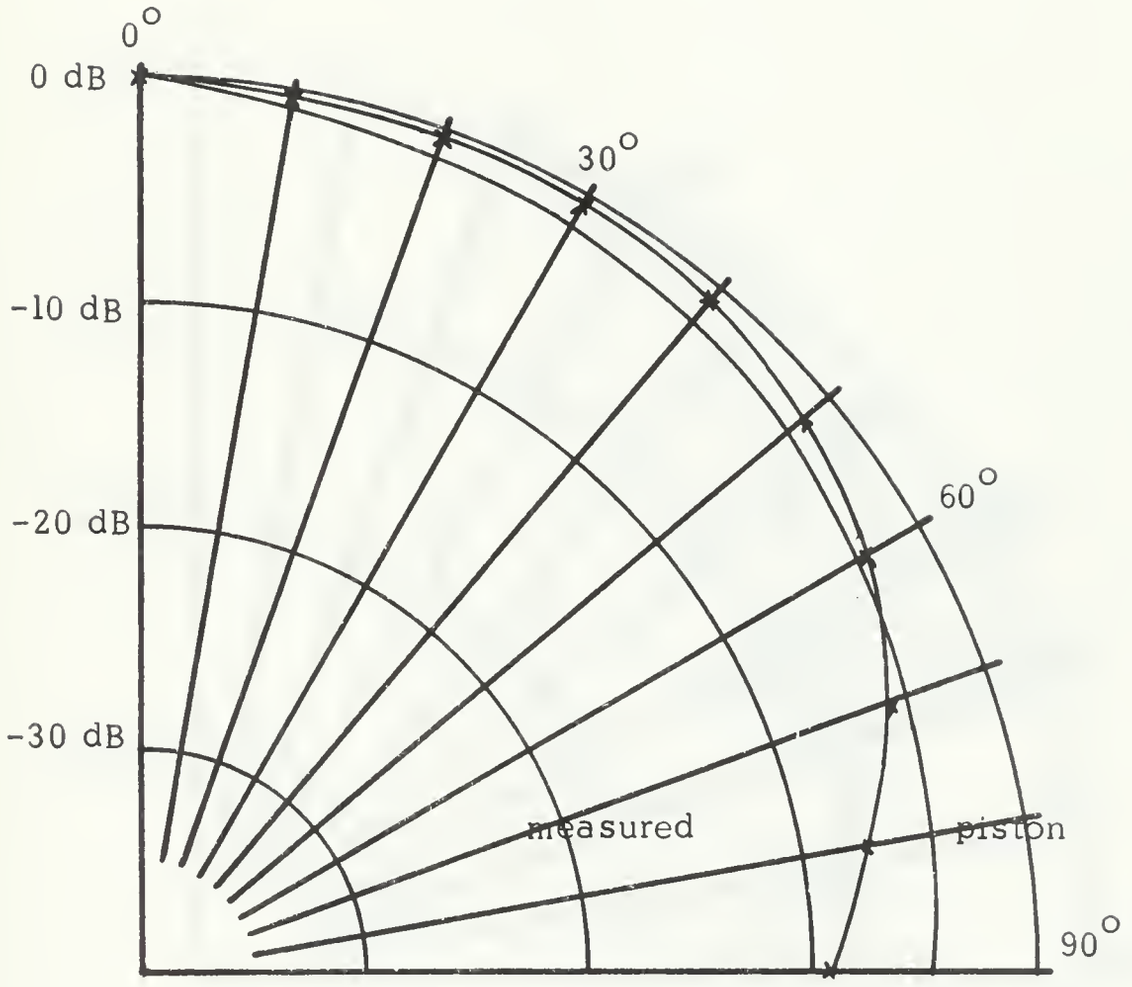

Fig. 30 Pressure Distribution for 23.0 KHz

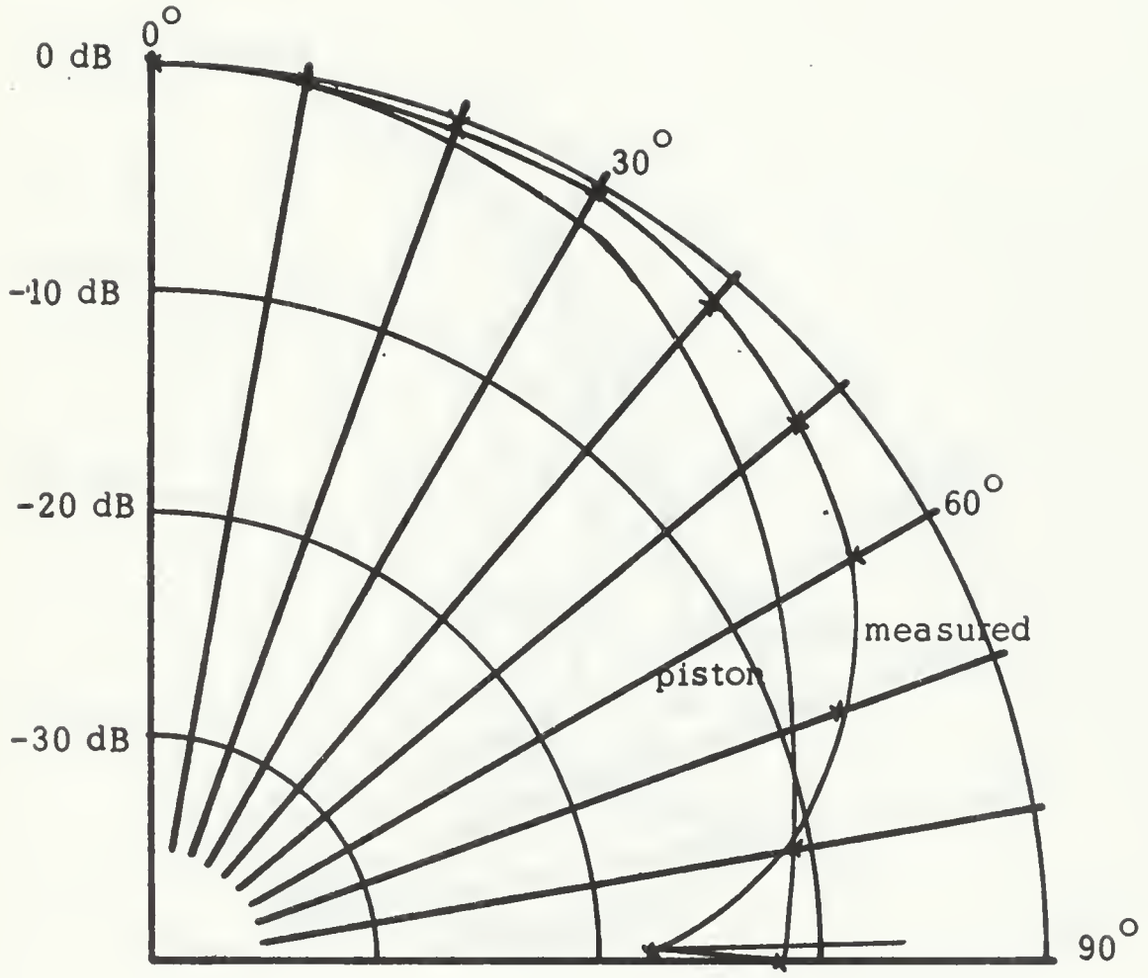

Fig. 31 Pressure Distribution for 30.0 KHz

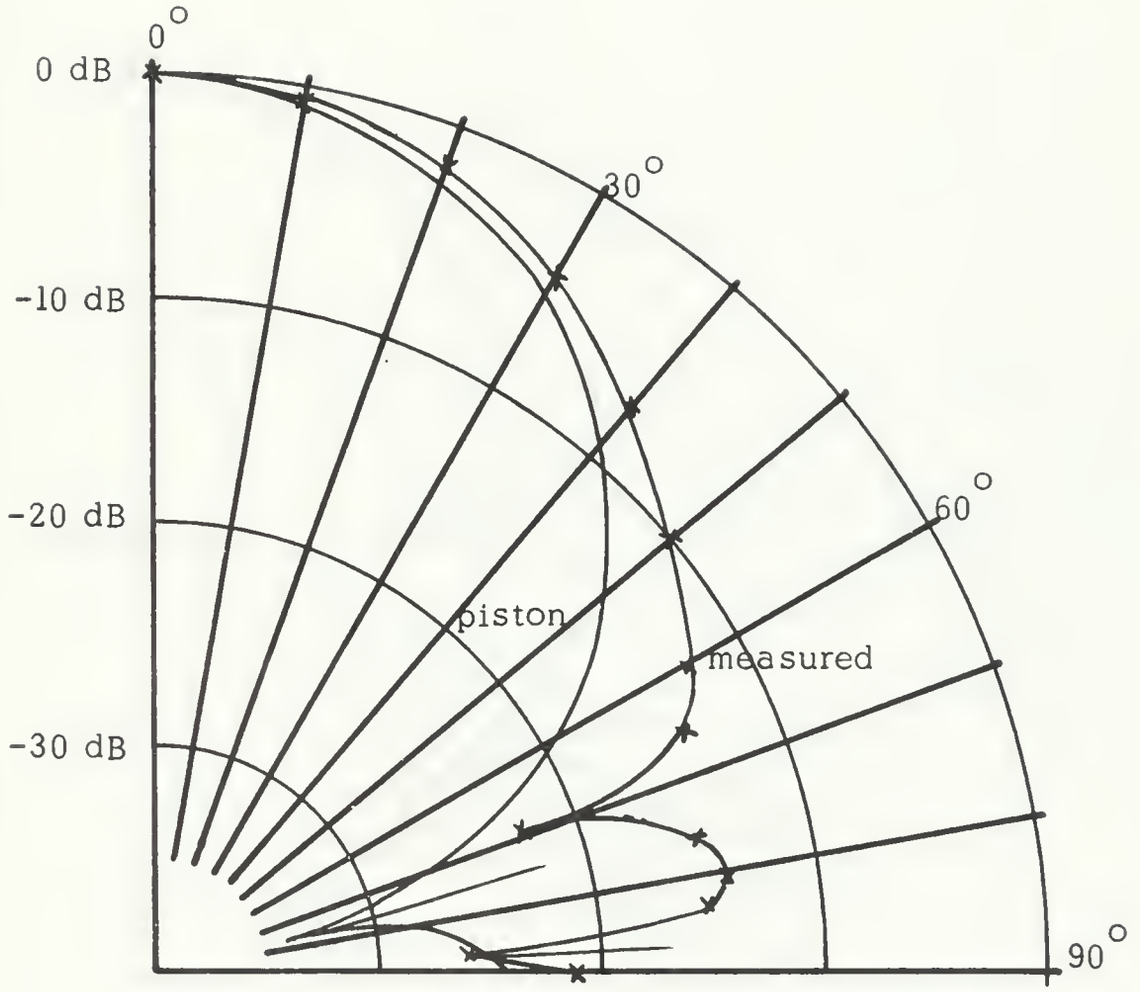

Fig. 32 Pressure Distribution for 47.5 KHz

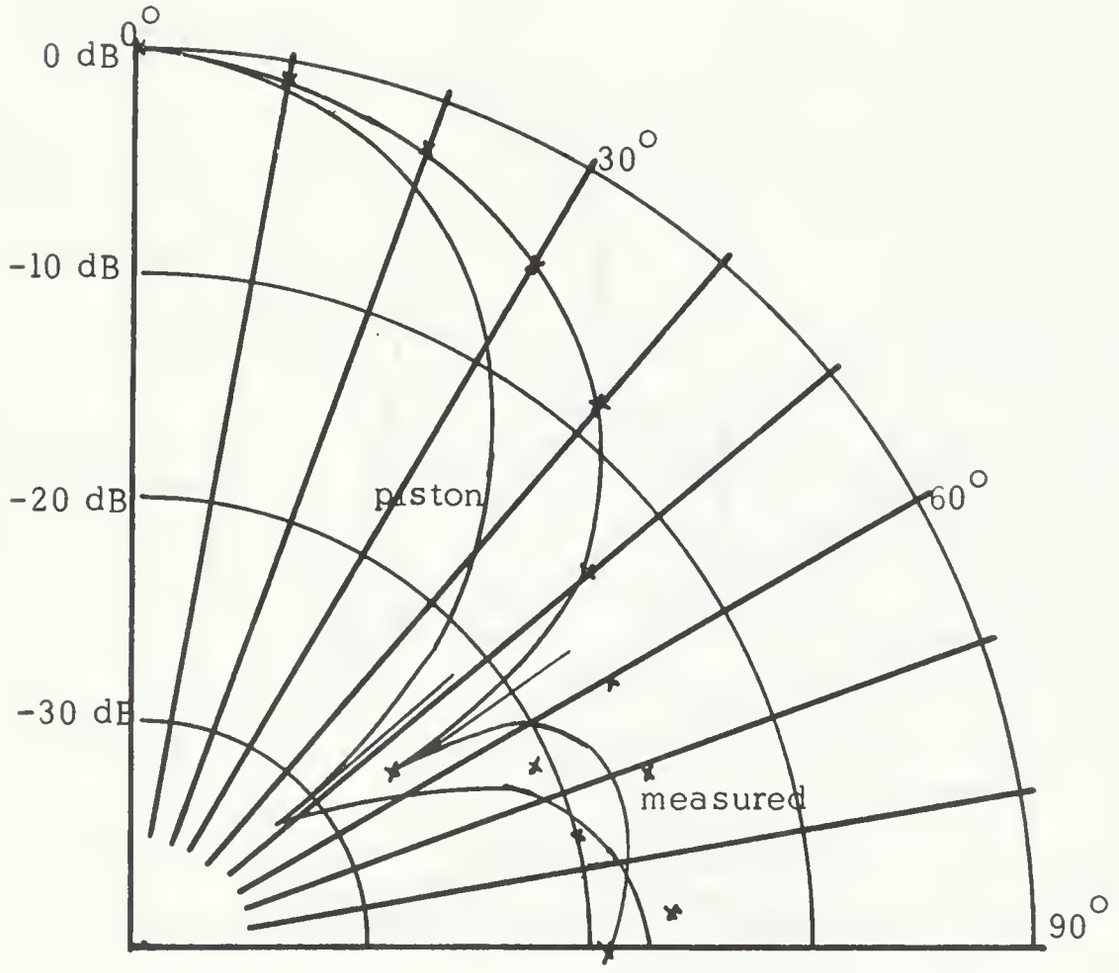

Fig. 33 Pressure Distribution for 61.5 KHz

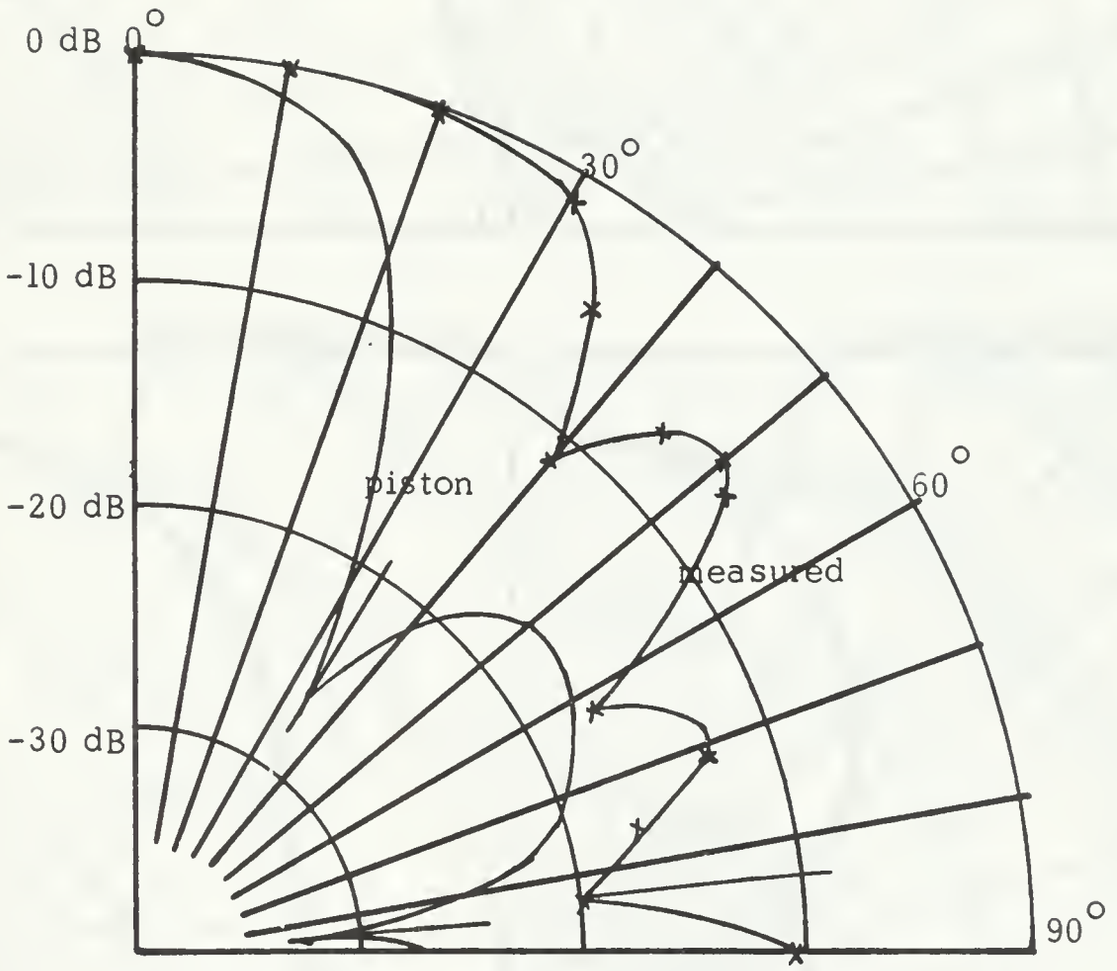

Fig. 34 Pressure Distribution for 87.5 KHz

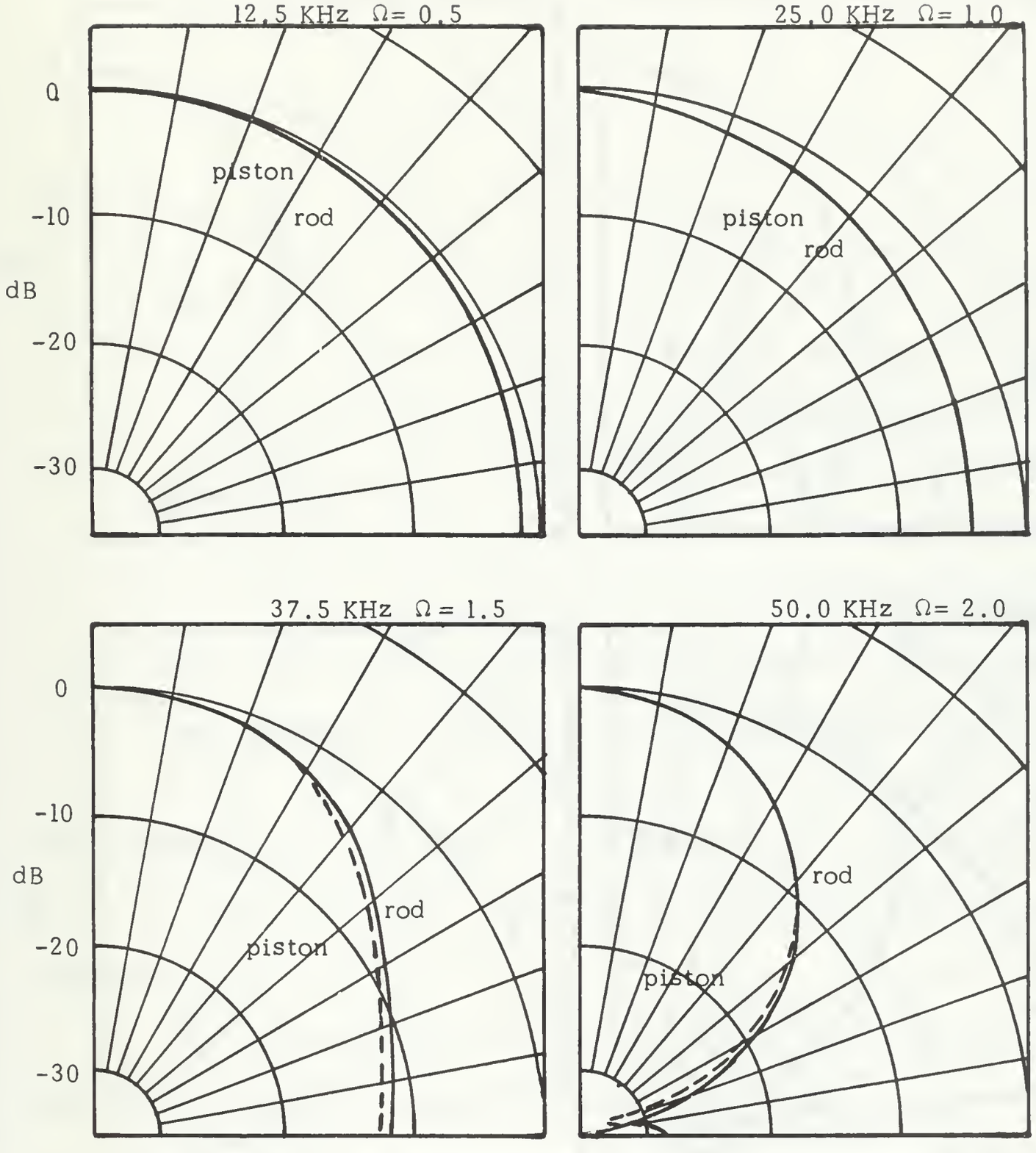

Fig. 35 Predicted Radiation Patterns for Rod and Piston for Frequencies 12.5 - 50.0 KHz

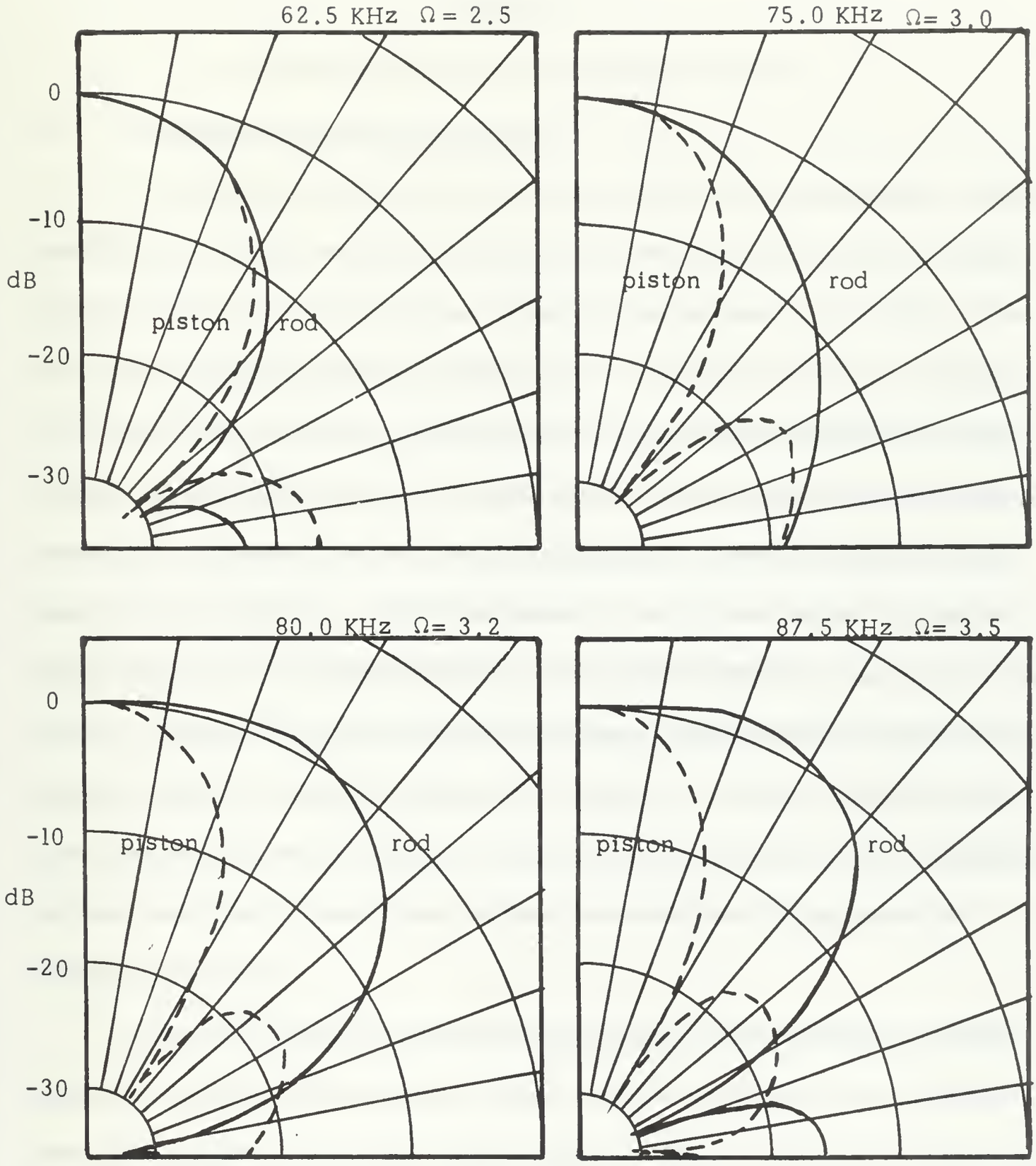

Fig. 36 Predicted Radiation Patterns for Rod and Piston for Frequencies 62.5 - 87.5 KHz

CHAPTER V

CONCLUSIONS AND RECOMMENDATIONS

A. Summary of Experimental Results

The results of this experiment were qualitatively as expected. Radial distribution of axial particle displacement at the radiating surface of a cylindrical rod were shown to be dome shaped for frequencies up to 30 KHz. The dome shaped displacement was made up of a component of uniform displacement added to a component of deformation. As frequency increased the component of uniform displacement decreased while the component of deformation increased. Maximum peak-to-peak displacement observed during this work was about 2.0 microns. "Nodal cylinders" of axial displacement in the rod developed near 29 KHz and existed for all higher frequencies examined in this project. Between 29 and 47.5 KHz the minimum displacement on the rod face moved toward the centerline and became smaller. The same pattern repeated itself between 50 and 85.8 KHz. Additionally displacement at the cylindrical surface was found to grow larger relative to centerline displacement as frequency increased.

Results of directivity pattern measurements were implied by the displacement profile measurements. At low frequency (10 KHz) pressure distribution was quite similar to that of the piston approximation. As the dome shape on the radiating face became more prominent, with higher frequencies, the reduction in effective radiating area caused slightly greater beam width than predicted by the piston approximation. The beam width itself was shown to decrease with increasing frequency. At a frequency corresponding to development of a

"nodal cylinder" of axial displacement a second lobe began to appear in the radiation pattern. With increasing frequency the number of side lobes increased while their nodes progressed angularly toward the axial centerline of the rod. A maximum of three side lobes were observed at 87.5 KHz with nodal pressures at 40°, 60°, and 83° from the centerline and having 12, 17, and 20 decibel dips relative to axial pressure.

B. Areas for Fruitful Further Research

In the course of this work various difficulties experienced and results obtained have pointed to other areas where work is needed. A good technique for obtaining quantitative dynamic measurements of plane piston motion is needed. Perhaps more work with the attached membrane method attempted by the author would provide the necessary technique. Certainly the results of an experiment such as this are dependent upon the amount of energy that can be put into the rod since the accuracy of measurements is a function of the total peak-to-peak displacement on the rod end. To alleviate this problem a larger source of undistorted sinusoidal power is needed over a wide band of frequencies.

It is felt that the greatest need for further research in this area is in the resolution of discrepancies between experimental results and existing theory. As yet the theoretical rod problem has not been extended to the case of a finite rod.

APPENDIX I

DIGITAL PROGRAM "FIELDS"

Included in the program listing for "FIELDS" are the basic program and various subroutines necessary to compute, tabulate, and plot axial velocity profile, pressure distribution for a plane piston, and pressure distribution for the actual rod problem. Additionally, longitudinal stress distribution across the rod is computed and tabulated with the "FIELDS" program. In the velocity and pressure segments both magnitudes and phases are tabulated and plotted.

Fortran variables which must be supplied on data cards are listed and defined below:

IP - A call for punched output; punched output if set at one, no punched output if set at zero.

SG - Specific gravity of the rod

PR - Poisson's ratio for the rod material

G - Shear modulus of the rod

RHO - Density of the rod

CWAT - Propagation speed of sound in the fluid

N - Number of data points across the rod radius

LL - Number of branches used in the computation

RAD - Radius of the rod

MODE - Code number for automatic frequency incrementation; no incrementation when set to 3

L2 - An unused variable in this program

KRNPRNT - A call for values computed by subprogram KERNAL; values not printed if set at 0, values printed if set at 1

SIRF - Non-dimensional radial position (initial)

SIRD - Radial position increment

SIRL - Non-dimensional radial position (final)

WWF - First incremented non-dimensional frequency; not used if MODE = 3

WWD - Increment of non-dimensional frequency; not used if MODE = 3

WWL - Last incremented non-dimensional frequency; not used if MODE = 3

THETF - First angular position for pressure computation

THETD - Increment in angular position

THETL - Last angular position for pressure computation

GAMF - First non-dimensional source point to field point distance

GAMD - Increment of non-dimensional source point to field point distance

GAML - Last non-dimensional source point to field point distance

```
                PROGRAM FIELDS(INPUT,OUTPUT,PUNCH)
000002          COMMON/B/BEMW
000002          COMMON/DATA/W,EPS,MODE,RAD,RAD2,LL,SG
000002          COMPLEX PW,BW
000002          DIMENSION B(50),S(50),P(50),B2(50),S2(50),R(50),Q(50),DISP(99),VDI
                1ST(99),SS(99),LSTRS(99),VMAG(99),PRES(99),PMAG(99),THETAN(99),VPHS
                1(99),PPHS(99),TITL(6),PW(50),BW(50)
000002          COMMON/PNT/KRNPRNT
000002          INTEGER VSCA
000002          COMPLEX B,S,P,B2,S2,R,PRES,IN,CSQRT,J0P,J1P,J0S,J1S,Q,DISP,VDIST,L
                1STRS,CABS
000002          COMPLEX VAL,VELSUM,ZRAD,VEL
000002          COMMON/PR/B,P,S,B2,S2,R,Q,DISP,VDIST,SS,PW,BW
000002          COMMON/COOR/SIRF,SIRD,SIRL
000002          PI=3.14159265
000003          CONV=PI/180.
000005          PRINT 40
000011          READ 706,SG,IP
000021      706 FORMAT(F10.2,I5)
000021          PRINT 707,SG,IP
000031      707 FORMAT(5X,*SPECIFIC GRAVITY OF SOLID=*,F15.5,5X,*IP=*I5)
000031          READ 700,PR,G,RHO,CWAT
000045      700 FORMAT(4F20.3)
000045          DE2=(1.-2.*PR)/(2.-2.*PR)
000051          CS=SQRT(G/RHO)
000055          EPS=CS/CWAT
000057          DELTA=SQRT(DE2)
000062          PRINT 710,PR,G,RHO,CWAT,DE2,CS,EPS
000103      710 FORMAT(1X,*PR,G,RHO,CWAT,DE2,CS,EPS*,7E14.5)
000103          READ 10,       N,LL,RAD,MODE,L2,    KRNPRNT
000123       10 FORMAT(       2I10,F10.7,2I10,       I5)
000123          RAD2=RAD*RAD
000124          NN=N
000126       16 FORMAT(1X,*RANGES FOR RADIAL COORD FOR STRESS* 3F20.5)
000126          READ 19 ,SIRF,SIRD,SIRL
000140       19 FORMAT(3F20.5)
000140          PRINT 19 ,SIRF,SIRD,SIRL
000152          READ 20,WWF,WWD,WWL
000164          IF(MODE.EQ.1)W=WWF
000170          READ 20,THETF,THETD,THETL
000202       20 FORMAT(3F20.8)
000202          READ 30,GAMF,GAMD,GAML
000214       30 FORMAT(3F20.6)
000214          PRINT 40,       N,RAD,LL,MODE,L2,    KRNPRNT
000234       40 FORMAT(1X,                5X,*N=*I5,5X,*RAD=*F10.6,5X,*LL=*I10,5X,*M
                1ODE=*I5,5X,*L2=*I5,/,5X,                5X,*KRNPRNT=*I5)
000234          PRINT 50,THETF,THETD,THETL
000246       50 FORMAT(5X,*THETA RANGES*,3F20.6)
000246          PRINT 60,GAMF,GAMD,GAML
000260       60 FORMAT(5X,*GAMMA RANGES*,3F20.6)
000260          NTIMES =0
000261          THETF=THETF*CONV    $    THETD=THETD*CONV     $   THETL=THETL*CONV
000265          ZTA=-GAM
000266       59 CONTINUE
000266          THETA=THETF
000267          GAM=GAMF
000271          IF(MODE.EQ.1)GO TO 300
000273          NTIMES=NTIMES+1
```

```
000274          GO TO (33,31,38)NTIMES
000303       33 CONTINUE
000303          GO TO 36
000304       31 CONTINUE
000304          MODE=2
000305          GO TO 300
000306       38 NTIMES=1
000307       36 CONTINUE
000307          READ 70,W
000315       70 FORMAT(F10.5)
000315          IF(W.EQ.0.)RETURN
000320       39 CONTINUE
000320          PRINT 80,W
000326       80 FORMAT(5X,*W=*F10.5)
000326          READ 90,(B(L),L=1,LL)
000335       90 FORMAT(2F15.10)
000335          PRINT 95
000341       95 FORMAT(15X,*B(L)*)
000341          PRINT 110,(B(L),L=1,LL)
000350      110 FORMAT(1X,4(2F15.10))
000350      140 READ 130,(R(L),L=1,LL)
000357      130 FORMAT(2F20.10)
000357          PRINT 149
000363      149 FORMAT(15X,*REFLECTION COEFFICIENTS*)
000363          PRINT 150,(R(L),L=1,LL)
000372      150 FORMAT(1X,4(2F15.10))
000372      300 CONTINUE
000372          SID=1./N
000374          TO=2.*PI/N
000377          W2=W*W
000401          W3=W2*W
000402          IF(MODE.EQ.1)GO TO 800
000404          IF(NTIMES.EQ.2)GO TO 333
000406          DO 160 L=1,LL
000410          B2(L)=B(L)*B(L)
000417          P(L)=CSQRT(CE2*W2-B2(L))
000434          S(L)=CSQRT(W2-B2(L))
000447          S2(L)=S(L)*S(L)
000456          CALL BSLJ(P(L),J0P,J1P)
000461          CALL BSLJ(S(L),J0S,J1S)
000467          C(L)=J1P/J1S
000476          PW(L)=2.*P(L)*P(L)-W2
000507          BW(L)=2.*B2(L)-W2
000515      160 CONTINUE
000520          JG=0
000520          I=1
000521          SI=0.
000522       22 CONTINUE
000522          CALL VELOC(SI,I,VEL)
000525          IF(JG.GE.NN)799,23
000532       23 I=I+1
000534          JG=JG+1
000535          SI=SI+SID
000537          GO TO 22
000537      799 CONTINUE
000537          NTYPE=1
000540          KJ=5
000541          TITL(1)=7HVELOCIT
```

```
000542          TITL(2)=7HY PROFI
000544          TITL(3)=7HLE
000546          TITL(4)=TITL(5)=TITL(6)=7H
000551          NABSKP=1
000552          VSCA=50    $  JUMP=1    $    LIN=1    $    NP=N+1
000557          DO 350    I=1,NP
000560      350 VMAG(I)=CABS(VDIST(I))
000570          CALL PLTLL(VMAG,SS,VSCA,JUMP,NP,LIN,NABSKP,KJ,NTYPE,TITL,W)
000603          CALL PHS(VDIST,VPHS,NP)
000606          TITL(1)=7HVELOCIT
000607          TITL(2)=7HY PHASE
000611          TITL(3)=7H
000613          CALL PLTLL(VPHS,SS,VSCA,JUMP,NP,LIN,NABSKP,KJ,NTYPE,TITL,W)
000625          PRINT 480
000631      480 FORMAT(*1*)
000631          PRINT 1000,W
000637     1000 FORMAT(15X,*VELOCITY AND DISPLACEMENT DISTRIBUTION FOR W=*F10.3)
000637          NLIMIT=N+1
000641          PRINT 1008
000645     1008 FORMAT(/,15X,*SI*,23X,*VELOCITY*,20X,*VMAG*,8X,*VPHS*  /)
000645          DO 1009 IJ=1,NLIMIT
000647     1009 PRINT 1020,SS(IJ),VDIST(IJ),VMAG(IJ),VPHS(IJ)
000666     1020 FORMAT(5X,F15.7,5X,2E15.6,5X,2E15.6)
000666      333 CONTINUE
000666          K=1
000667      800 CONTINUE
000667          CALL MULTINT(GAM,IN,PI,N,NN,SID,TD,THETA)
000677          PRES(K)=(0.,1.)*W2*IN/(2.*PI*SG)
000714          THETAN(K)=THETA/CONV
000715          K=K+1
000720          THETA=THETA+THETD
000721          IF(THETA.GT.THETL)201,800
000725      201 IF(MODE.EQ.1)205,200
000732      205 W=W+WWD
000733          W2=W*W
000734          IF(W.GT.WWL)210,230
000741      210 W=WWF     $GAM=GAM+GAMD    $  THETA=THETF    $  W2=W*W
000747          IF(GAM.GT.GAML)RETURN
000753          GO TO 800
000754      230 THETA=THETF
000756          PRINT 1010,W
000763     1010 FORMAT(25X,*W=*F10.3)
000763          GO TO 800
000764      200 CONTINUE
000764          NTYPE=2
000765          KJ=6
000766          K=K-1
000770          CALL BEEM(K,THETD,PRES)
000772       69 FORMAT(I5)
000772          JUMP=1
000773          TITL(1)=7HPRESSUR
000774          TITL(2)=7HE DISTR
000776          TITL(3)=7HIBUTION
001000          GO TO(8000,8010)NTIMES
001006     8000 TITL(4)=7H FOR UN
001007          TITL(5)=7HIFORM V
001011          TITL(6)=7HELOCITY
001013          GO TO 8020
```

```
001013     8010 TITL(4)=7H FOR RO
001014          TITL(5)=7HD PROBL
001016          TITL(6)=7HEM
001020     8020 CONTINUE
001020          NABSKP=1
001021          DO 360 I=1,K
001023      360 PMAG(I)=CABS(PRES(I))
001034          CALL PLTLL(PMAG,THETAN,VSCA,JUMP,K,LIN,NABSKP,KJ,NTYPE,TITL,W)
001046          CALL PHS(PRES,PPHS,K)
001051          TITL(1)=7HPRESSUR
001052          TITL(2)=7HE PHASE
001054          TITL(3)=7H
001056          CALL PLTLL(PPHS,THETAN,VSCA,JUMP,K,LIN,NABSKP,KJ,NTYPE,TITL,W)
001070          PRINT 480
001074          PRINT 180,W
001102      180 FORMAT(10X,*PRESSURE AND PHASE FOR W=*F10.3//)
001102          PRINT 185
001106      185 FORMAT(15X,*THETA*,20X,*PRESSURE*,20X,*PMAG*,8X,*PPHS*  /)
001106          DO 186 I=1,K
001110      186 PRINT 187,THETAN(I),PRES(I),PMAG(I),PPHS(I)
001127      187 FORMAT(5X,F15.2,5X,2E15.6,5X,2E15.6)
001127          GAM=GAM+GAMC
001130          IF(GAM.GE.GAML)58,220
001135       58 CONTINUE
001135          IF(NTIMES.EQ.2) GO TO 59
001137          PRINT 639
001143      639 FORMAT(////)
001143          PRINT 640,W
001151      640 FORMAT(25X,*STRESS FOR W=*F10.5/10X,*IJI*,20X,*LONG. STRESS*)
          C   WILL WANT TO ADD A STATEMTNET HERE FOR INCREMENTING GAMMA IF USE
          C   MORE THAN ONE GAMMA
001151          CALL STRESS(GAM,LSTRS,IST)
001154          IST=IST-1
001156          DO 667 IJI=1,IST
001157      667 PRINT 666,IJI,LSTRS(IJI)
001172      666 FORMAT(8X,I5,10X,2E20.6)
001172          GO TO 59
001172      220 THETA=THETF
001174          GO TO 800
001174          END
                SUBROUTINE STRESS(GAM,LSTRS,IST)
000005          COMMON/DATA/W,EPS,  MODE,RAD,   RAD2,LL
000005          DIMENSION LSTRS(99)
000005          COMMON/PR/B(50),P(50),S(50),B2(50),S2(50),R(50),Q(50),DISP(99),VDI
               1ST(99),SS(99) ,PW(50),BW(50)
000005          COMMON/COOR/SIRF,SIRD,SIRL
000005          COMPLEX B,P,S,B2,S2,R,Q,DISP,VDIST,LSTRS,E,D,FAC,CEXP,J0PS,J1PS,J0
               1SS,J1SS,PW,BW
000005          SI=SIRF
000006          IST=1
000007          LSTRS(IST)=(0.,0.)
000013          GNE=-GAM
000014        1 CONTINUE
000014          DO 10 L=1,LL
000017          D=4.*S(L)*P(L)*B2(L)*Q(L)/(B2(L)-S2(L))
000047          E=2.*P(L)*P(L)-W*W
000061          IF(L.EQ.1) 15,20
000064       15 FAC=CEXP(-(0.,1.)*B(L)*GNE)-R(L)*CEXP((0.,1.)*B(L)*GNE)
000124          GO TO 25
000126       20 FAC=-R(L)*CEXP((0.,1.)*R(L)*GNE)
000152       25 CALL BSLJ(P(L)*SI,J0PS,J1PS)
000162          CALL BSLJ(S(L)*SI,J0SS,J1SS)
000174       10 LSTRS(IST)=LSTRS(IST)+(J0PS*E-D*J0SS)*FAC
000223          IST=IST+1
000224          IF(SI.GE.SIRL)RETURN
000230          SI=SI+SIRD
000232          LSTRS(IST)=(0.,0.)
000236          GO TO 1
000236          END
```

```
                SUBROUTINE KERNEL(SI,THETA,GAM,KRNL,PHI,I)
000010          COMMON/PR/B,P,S,B2,S2,R,Q,DISP,VDIST,SS,PW,BW
000010          COMMON/DATA/W,EPS,  MODE,RAD,   RAD2,LL
0000 10         DIMENSION B(50),S(50),P(50),B2(50),S2(50),R(50),Q(50),DISP(99),VDI
               1ST(99),SS(99),LSTRS(99),PW(50),BW(50)
000010          COMPLEX B,S,P,B2,S2,R,PRES,IN,CSQRT,J0P,J1P,J0S,J1S,Q,DISP,VDIST,L
               1STRS,PW,BW
000010          COMPLEX CEXP,KRNL,VEL,CABS
000010          IF(MODE.EQ.3) 10,20
000013       10 VEL=VDIST(1)
000016          GO TO 25
000016       20 VEL=(0.,0.)
000021          VEL=VDIST(I)
000024       25 CONTINUE
000024          SIG=SQRT(GAM*GAM*SI*SI-2.*GAM*SI*SIN(PHI)*COS(THETA))
000053          KRNL=SI*VEL*CEXP(-(0.,1.)*W*EPS  *SIG)/SIG
000102          RETURN
000102          END



                SUBROUTINE VELOC(SI,I,VEL)
000005          COMMON/PR/B,P,S,B2,S2,R,Q,DISP,VDIST,SS, PW,BW
000005          COMPLEX PW,BW,CEXP
000005          COMMON/DATA/W,EPS,  MODE,RAD,   RAD2,LL
000005          DIMENSION DISP(99),VDIST(99),SS(99),P(50),B(50),S(50),B2(50),S2(50
               1),R(50),Q(50),PW(50),BW(50)
000005          COMPLEX VEL,DISP,VDIST,J0PS,J1PS,J0SS,J1SS,C,D,FAC,B,P,S,B2,S2,R,Q
000005          GO TO(10,20,20),MODE
000014       10 VEL=(1.,0.)
000017          RETURN
000017       20 VEL=(0.,0.)
000022          ZTA=-1.E-10
000023          DO 30 L=1,LL
000025          CALL BSLJ(P(L)*SI,J0PS,J1PS)
000034          CALL BSLJ(S(L)*SI,J0SS,J1SS)
000045          FAC=CEXP((0.,1.)*B(L)*ZTA)
000060          D=2.*P(L)*S(L)*Q(L)/BW(L)
000107          C=B(L)*(J0PS+D*J0SS)
000126          IF(L.EQ.1)50,60
000133       50 VEL=C/FAC
000142       60 VEL=VEL+C*R(L)*FAC
000156       30 CONTINUE
000161          SS(I)=SI
000162          VDIST(I)=VEL
000165          DISP(I)=-(0.,1.)*VEL
000173          RETURN
000173          END
```

```
                SUBROUTINE MULTINT(GAM,IN,PI,N,NN,SID,TD,FLDANG)
000012          DIMENSION K(110),SUM(110)
000012          COMMON/PNT/KRNPRNT
000012          REAL LMT
000012          COMPLEX IN,K,KRNL,SUM,GSUM
                C       COMPUTES   (IN)  AS A FUNCTION OF GAM AND FLDANG
000012          THETA=SI=0.
000014          GSUM=(0.,0.)
000016          JG=0
000017          JT=0
000020          J=1
000021          SUM(J)=(0.,0.)
000024        1 CONTINUE
000024          I=1
000025        2 CONTINUE
000025          CALL KERNEL(SI,THETA,GAM,KRNL,FLDANG,T)
000032          K(I)=KRNL
000036          IF(JG.GE.NN)5,10
000047       10 I=I+1
000051          JG=JG+1
000052          SI=SI+SID
000053          GO TO 2
000054        5 CONTINUE
000054          IF(KRNPRNT.EQ.1)3,4
000060        3 PRINT 6
000064        6 FORMAT(15X,*KRNL*)
000070          PRINT 7,(K(JJ),JJ=1,I)
000076        7 FORMAT(5X,4(2E15.5))
000102        4 CONTINUE
000102          SUM(J)=K(1)+K(I)
000111          II=3
000112       30 CONTINUE
000112          SUM(J)=SUM(J)+2.*K(II)
000126          IF(II.GE.(I-2)) 35,40
000133       40 II=II+2
000135          GO TO 30
000135       35 II=2
000136       36 SUM(J)=SUM(J)+4.*K(II)
000152          IF(II.GE.(I-1))45,50
000157       50 II=II+2
000161          GO TO 36
000161       45 IF(JT.GE.N)55,60
000166       60 CONTINUE
000166          THETD=THETA*180./PI
000170          J=J+1          SI=0.
000173          JG=0
000173          THETA=THETA+TD
000175          JT=JT+1
000176          GO TO 1
000177       55 GSUM=SUM(1)+SUM(J)
000205          II=3
000206       75 CONTINUE
000206          GSUM=GSUM+2.*SUM(II)
000217          IF(II.GE.(J-2))80,85
000225       85 II=II+2
000227          GO TO 75
000227       80 II=2
000230       81 GSUM=GSUM+4.*SUM(II)
000241          IF(II.GE.(J-1))90,95
000247       95 II=II+2
000251          GO TO 81
000251       90 IN=GSUM*TD*SID/9.
000260          RETURN
000260          END
```

```
      SUBROUTINE PLTLL(REF,ABC,VSCA,JUMP,LL,LIN,NABSKP,KJ,NTYPE,TITL,W)
C   PLOTS REF AS A FUNCITON OF ABC
C   VSCA IS VERTICAL SCALE
C   JUMP IS HORIZONTAL SPACE BETWEEN DATA POINTS
C   MINUS ONE
C   LL IS DIMENSION OF REF
C   LIN IS LINEAR FLAG, IF EQUAL TO ONE GET LINEAR PLOT,OTHERWISE GET
C  LOGARITHMIC PLOT
C  NTYPE =1    IF VELOCITY PLOT
C   NTYPE =2    IF PRESSURE PLOT
000015        INTEGER VSCA
000015        COMMON/B/BW
000015        REAL MPR
000015        DIMENSION REF(99),ABC(99),MPR(75,100),IS(99),TITL(6)
000015        PRINT 1000
000020        PRINT 250,(TITL(I),I=1,6)
000031    250 FORMAT(40X,6A7,/)
000035        IF(NTYPE.EQ.2)PRINT 900,BW
000050    900 FORMAT(50X,*BEAM WIDTH=*F10.3)
000050        IF(LIN.EQ.1)600,620
000053    600 PRINT 630,W
000061    630 FORMAT(40X,*LINEAR PLOT*,15X,*W=*F8.2)
000065        GO TO 650
000065    620 PRINT 625,W
000073    625 FORMAT(40X,*LOGARITHMIC PLOT*,10X,*W=*F8.3,/)
000077    650 CONTINUE
000077        PLTSCAL=1.E2
000100        NN=LL*JUMP+3
000103        MM=VSCA+3
000105        DO 10 M=1,MM
000106        DO 10 N=1,NN
000116     10 MPR(M,N)=1H
C    FIND MAXIMUM AND MINIMUM OF REF
000126        IF(LIN.EQ.1)GO TO 401
000127        RMIN1=30.
000131        DO 3 I=1,LL,NABSKP
000132        IF(REF(I).LT.RMIN1)RMIN1=REF(I)
000136     3 CONTINUE
C     FIX DATA TO GET LOG PLOT
000142        DO 400 I=1,LL,NABSKP
000147        REF(I)=PLTSCAL*ALOG10(REF(I)/RMIN1)
000161    400 CONTINUE
000163    401 CONTINUE
000163        RMIN=1.E10
000164        RMAX=0.
000165        DO 20 I=1,LL,NABSKP
000173        IF(REF(I).GT.RMAX)RMAX=REF(I)
000176        IF(REF(I).LT.RMIN)RMIN=REF(I)
000201     20 CONTINUE
000202        RANGE=ABS(RMAX-RMIN)
C    LOOC MATRIX WITH DATA  (SCALED)
000205        J=3
000206        DO 40 I=1,LL,NABSKP
000221        M=VSCA-((REF(I)-RMIN)/RANGE)*(VSCA-1)
000226        MPR(M+1,J)=1HX
000233        J=J+JUMP
000234     40 CONTINUE
C     SET UP HORIZONTAL BORDERS OF PLOT
```

```
000237          M=1    $    MB=VSCA+2
000245          DO 45 N=2,NN
000246       45 MPR(M,N)=MPR(MB,N)=1H-
           C     LABEL VERTICAL AXIS
000261          DELTA=RANGE/(VSCA-1.)
000264          TEMP=RMAX+DELTA
000265          N=1
000267          DO 65 I=1,VSCA
000305          M=I+1
000306          TEMP=TEMP-DELTA
000310          MPR(M,N)=TEMP
000310          IF(LIN.EQ.1)GO TO 65
000312          MPR(M,N)=RMIN1*10.**(MPR(M,N)/PLTSCAL)
000320       65 CONTINUE
           C    LABEL VERTICAL BORDERS OF PLOT
000325          N=2
000326          K=N+LL+JUMP+1
000332          DO 70 M=1,MM
000343          MPR(M,N)=1HI
000344       70 MPR(M,K)=1HI
000346          MM=MM-2
000350          M=1
000351     1000 FORMAT(*1*)
000355          PRINT 109 ,(MPR(M,N),N=1,NN)
000374      109 FORMAT(34X,70A1)
000400          DO 110 M=2,MM
000401          PRINT 120,MPR(M,1),(MPR(M,N),N=2,NN)
000422      120 FORMAT(20X,E15.5,70A1)
000426      110 CONTINUE
000430          M=VSCA+2
000431          PRINT 109 ,(MPR(M,N),N=1,NN)
000451          IF(NTYPE.EQ.1)320,300
000460      320 DO 130 I=1,LL,KJ
000467      130 IS(I)=ABC(I)*10.0001
000471          PRINT 131,(IS(I),I=1,LL,KJ)
000515      131 FORMAT(32X,1815)
000521          RETURN
000521      300 PRINT 310,(ABC(I),I=1,LL,KJ)
000543      310 FORMAT(31X,16F6.0)
000547          PRINT 132
000552      132 FORMAT(1X,///)
000556          PRINT 800,RMAX,RMIN,RMIN1
000567      800 FORMAT(5X,*RMAX=*E15.5,5X,*RMIN=*E15.5,*RMIN1=*E15.5)
000573          RETURN
000573          END
                SUBROUTINE PHS(VDIST,VPHS,NP)
000005          COMPLEX VDIST
000005          DIMENSION VDIST(99),VPHS(99)
000005          PI=3.1415926535
000006          CONV=PI/180.
000010          DO 451 I=1,NP
000012          CM=AIMAG(VDIST(I))
000013          RE=REAL(VDIST(I))
000014          IF(RE.GE.0..AND.CM.GE.0.)452,455
000024      452 VPHS(I)=ATAN(CM/RE)/CONV     $  GO TO 451
000035      455 IF(RE.LT.0..AND.CM.GT.0.)460,465
000044      460 VPHS(I)=180.+ATAN(CM/RE)/CONV    $    GO TO 451
000056      465 IF(RE.LT.0..AND.CM.LT.0.)470,475
000065      470 VPHS(I)=-180.+ATAN(CM/RE)/CONV     $  GO TO 451
000077      475 IF(RE.GT.0..AND.CM.LT.0.)VPHS(I)=360.+ATAN(CM/RE)/CONV
000117      451 CONTINUE
000122          RETURN
000122          END
```

```
                SUBROUTINE BEEM(K,THETD,PRES)
000005          COMMON/B/BW
000005          DIMENSION PRES(99)
000005          COMPLEX PRES,CABS
000005          PO=CABS(PRES(1))
000011          THETA=0.
000011          I=1
000013        1 CONTINUE
000013          RATIO=CABS(PRES(I))/PO
000026          IF(RATIO.LE.0.708)20,10
000033       10 I=I+1       $    THETA=THETA+THETD
000036          IF(I.GT.K)30,1
000042       30 PRINT 31,RATIO
000050       31 FORMAT(5X,*BEAM NEVER DROPS BELOW*E15.5*OF THE AXIAL PRESSURE*)
000052          BW=180.
000054          RETURN
000054       20 BW=2.*THETA*180./3.1415926535
000057          RETURN
000057          END
                SUBROUTINE BSLJ(Z,J0,J1)
000005          COMPLEX Z,J0,J1
000005          IF (CABS(Z) .GT.12.)1,2
000014       1  CALL ABESJ(Z,J0,J1)
000015          RETURN
000016       2  CALL PBESJ(Z,J0,J1)
000017          RETURN
000020          END
                SUBROUTINE PBESJ (Z,J0,J1 )
000005          COMPLEX Z,J0,J1, Z1, Z2, J0S, J1S, T1, T
000005          Z1 = .5*Z
000012          Z2 = Z1*Z1
000017          J0S= (0.,0.)
000022          J1S= (0.,0.)
000024          T1 = (.5,0.)
000027          H = 2.
000030       10 J1S = J1S + T1
000035          T1 = T1/H
000042          J0S = J0S + T1
000046          H = H + 1.
000050          T = T1*Z2
000056          T1 = - T/H
000063          IF(CABS(T1).GT.1.E-10) 10,20
000074       20 T = Z1*Z2
000102          T1 = T*J1S
000110          J1 = Z1 - T1
000114          T = Z2*Z2
000121          T1 = T*J0S
000127          J0 = (1.,0.) - Z2 + T1
000135          RETURN
000135          END
```

```
                SUBROUTINE ABESJ (Z, J0, J1 )
000005          TYPE COMPLEX Z,J0,J1,      RZ,RZ2,P0,P1,Q0,Q1,T0,T1,C1,CA,  Z1,RT,
               1             CSQRT,COZ,SIZ,ZCOZ,ZSIZ,U,       CC
000005          DIMENSION Z0(2),       Z10(2),C10(2)
000005          EQUIVALENCE(U,Z0),          (Z1,Z10),(C1,C10)
000005          U = Z
000007          X = ABS(Z0(1))
000011          Y = ABS(Z0(2))
000013          R = 8.*(X*X + Y*Y)
000016          Z10(1) = X
000017          Z10(2) = Y
000020          RZ = CONJG(Z1)/R
000027          RZ2 = RZ*RZ
000034          P0 = (0.,0.)
000037          P1 = (0.,0.)
000041          Q0 = (0.,0.)
000044          Q1 = (0.,0.)
000046          T0 = (1.,0.)
000051          T1 = (1.,0.)
000053          H = 1.
000054       10 P0 = P0 + T0
000061          P1 = P1 + T1
000065          C = 2.*H - 1.
000070          C = - C*C/H
000071          T0 = C*T0
000077          Q0 = Q0 + T0
000103          C = 4./H*C
000106          T1 = C*T1
000113          Q1 = Q1 + T1
000120          H = H + 1.
000121          A = 2.*H - 1.
000123          A = A*A/H
000124          CC = A*RZ2
000132          T0 = T0*CC
000140          A = -4./H + A
000143          CC = A*RZ2
000150          IF(CABS(C*CC).GT.1.) 20,11
000166       11 T1= CC*T1
000174          H = H + 1.
000176          IF(CABS(T1).GT.1.E-10) 10,20
000207       20 Q0= Q0*RZ
000215          Q1 = Q1*RZ
000223          RT = CSQRT(Z1)
000226          CA = .28209479177387A / RT
000235          DC = COS(X)
000236          DS = SIN(X)
000241          C10(1) = DC + DS
000243          C10(2) = DC - DS
000244          IF(Y.GT.25.)30,25
000253       25 E1 = EXP (Y)
000256          E2 = 1./E1
000257          COZ = C1*E1 + CONJG(C1)*E2
000271          SIZ = (0.,-1.)*(C1*E1 - CONJG(C1)*E2)
000311          GO TO 40
000314       30 COZ = C1*EXP(Y)
000323          SIZ = (0.,-1.)*COZ
000334       40 ZCOZ = CA*COZ
000342          ZSIZ = CA*SIZ
000350          J0 = P0*ZCOZ + Q0*ZSIZ
000363          J1 = - P1*ZSIZ + Q1*ZCOZ
000376          IF(Z0(1).GT.0.) 60,55
000402       55 J1 = - J1
000404       60 IF(Z0(1)*Z0(2).GT.0.) 70,65
000411       65 J0 = CONJG(J0)
000413          J1 = CONJG(J1)
000415       70 RETURN
000416          END
```

BIBLIOGRAPHY

1. P. M. Morse, Vibration and Sound, 2nd ed., McGraw Hill, Inc., New York, 1948.
2. R. B. Lindsay, Mechanical Radiation, McGraw Hill, Inc., New York, York, 1960.
3. Joseph Zemanek, Jr., "An Experimental and Theoretical Investigation of Elastic Wave Propagation in a Cylinder," Technical Report No. xvii, Dept. of Physics, U.S.L.A., April, 1962.
4. G. K. Miller, II, "Axisymmetric Stress-Wave Propagation Across the Common End Face Between Two Semi-infinite Cylinders, Solid to Fluid", J. Acoust. Soc. Am. 44, No. 4, 1040-1051.
5. G. G. Maxwell, "Acoustic Energy Transmission from a Rod into a Semi-infinite Medium", Ph.D. Dissertation, The University of Texas, Dept. of Elect. Eng., December, 1970.(To be published in J. Acoust. Soc. Am., Jan. 1972.)
6. L. J. Pockhammer, "Uber die Fortpflanzungeschwindigkeiten Kleiner Schwingungen in einem Unbegrenzten Isotropen Kreiszylinder", J. Riene u. angew. Math. 81, 324-336, 1876.
7. A.E.H. Love, A Treatise on the Mathematical Theory of Elasticity, Dover Publications, Inc., New York, 1892.
8. R.M. Davies, "A Critical Study on the Hopkinson Pressure Bar", Phil. Trans. Royal Soc. (London), A, 240, 375 (1948).
9. H. Kolsky, Stress Waves in Solids, Dover Publications, Inc., New York, 1963.

10. Enrico Volterra and E. C. Zachmanoglou, Dynamics of Vibrations, Charles E. Merrill Books, Inc., Columbus, Ohio, 1965.

11. L. E. Kinsler and A. R. Frey, Fundamentals of Acoustics, John Wiley and Sons, Inc., New York, 1962.

12. M. A. Monahan and K. Bromley, "Vibration Analysis by Holographic and Conventional Interferometry," Report No. 1513, Naval Electronics Laboratory Center, San Diego, California, September 8, 1969.

13. S. G. Varnado and A. H. LaGrone, "Theoretical and Experimental Study of the Spatial Coherence of Laser Radiation and its Application to Underwater Detection Systems", Antennas and Propagation Laboratory, Report No. P-36, The University of Texas, July 18, 1969.

VITA

Lionel Jerome Nowotny was born in New Braunfels, Texas, on August 9, 1938, the son of Hedwig Hildebrand Nowotny and Jerome Nowotny. After completing his work at New Braunfels High School in 1956, he entered The University of Texas, at Austin, Texas. In the spring of 1957 he received an appointment to the United States Naval Academy, at Annapolis, Maryland. He graduated, with distinction, from the United States Naval Academy in June, 1961, receiving a Bachelor of Science degree and a commission in the United States Navy. In 1961, he married Mary Lou Mueller of New Braunfels. Daughter, Sharon Elizabeth was born in 1963 and daughter, Julie Anna was born in 1966. During the six years following commissioning he served in the U. S. Navy Nuclear Submarine Forces. This service included two and one-half years as an instructor at the Navy Nuclear Power Training School, at Mare Island, California. In July, 1967, he entered graduate training at the U. S. Naval Postgraduate School, at Monterey, California. In June, 1969, he entered the Graduate School of the University of Texas at Austin. In December, 1971, he was elected to membership in Phi Kappa Phi, honorary scholastic fraternity. He currently holds the rank, Lieutenant Commander, United States Navy.

Permanent address: 212 W. Austin Street
New Braunfels, Texas 78130

This dissertation was typed by Shirley Thompson.

Thesis
N946 Nowotny
Measurement of axial velocity profiles and resulting acoustical fields of a rod.
131353

Thesis
N946 Nowotny
Measurement of axial velocity profiles and resulting acoustical fields of a rod.
131353

thesN946
Measurement of axial velocity profiles a
3 2768 001 94761 7
DUDLEY KNOX LIBRARY